

Segmentation of Photovoltaic Module Cells in Electroluminescence Images

Sergiu Deitsch · Claudia Buerhop-Lutz · Evgenii Sovetkin · Ansgar Steland · Andreas Maier · Florian Gallwitz · Christian Riess

Received: date / Accepted: date

Abstract High resolution electroluminescence (EL) images captured in the infrared spectrum allow to visually and non-destructively inspect the quality of photovoltaic (PV) modules. Currently, however, such a visual inspection requires trained experts to discern different kinds of defects, which is time-consuming and expensive. Automated segmentation of cells is therefore a key step in automating the visual inspection workflow.

In this work, we propose a robust automated segmentation method for extraction of individual solar cells from EL images of PV modules. This enables controlled studies on large amounts of data to understanding the effects of module degradation over time—a process not yet fully understood.

The proposed method infers in several steps a high-level solar module representation from low-level edge features. An important step in the algorithm is to formulate the segmentation problem in terms of lens calibration by exploiting the plumbline constraint. We evaluate our method on a dataset of various solar modules types containing a total of 408 solar cells with various defects. Our method robustly solves this task with a median weighted Jaccard index of 94.47% and an F_1 score of 97.54%, both indicating a very high similarity between automatically segmented and ground truth solar cell masks.

Keywords PV modules, EL imaging, visual inspection, lens distortion, solar cell extraction, pixelwise classification

1 Introduction

Visual inspection of solar modules using EL imaging allows to easily identify damage inflicted to solar panels either by environmental influences such as hail, during the assembly process, or due to prior material defects or material aging [53, 5, 73, 74, 3, 76]. The resulting defects can notably decrease the photoelectric conversion efficiency of the modules and thus their energy yield. This can be avoided by continuous inspection of solar modules and maintenance of defective units. For an introduction and review of non-automatic processing tools for EL images, we refer to Mauk [49].

An important step towards an automated visual inspection is the segmentation of individual cells from the solar module. An accurate segmentation allows to extract well-aligned solar cell images [7]. Such solar cell images are the ideal training data for classifiers to predict defects in solar modules [13]. In particular, samples fed into a Convolutional Neural Network (CNN) need to be correctly aligned since CNNs are in general not spatially invariant [36, 43]. The identification of solar cells is additionally required by the international technical specification IEC TS 60904-13 [34, Annex D] for further identification of defects on cell level. Finally, automated segmentation can also ease the development of models that predict the performance of a PV module based on detected or identified failure modes, or by determining the operating voltage of each cell [58]. The data describing the cell characteristics can be fed into an electric equivalent model that allows to estimate or simulate the current-voltage characteristic (I-V) curve [60, 8, 38] or even the overall power output [39].

The appearance of PV modules in EL images depends on a number of different factors, which makes an automated segmentation challenging. The appearance varies with the type of semiconducting material

S. Deitsch
Pattern Recognition Lab
University of Erlangen-Nuremberg
Martensstr. 3
91058 Erlangen, Germany
E-mail: sergiu.deitsch@fau.de

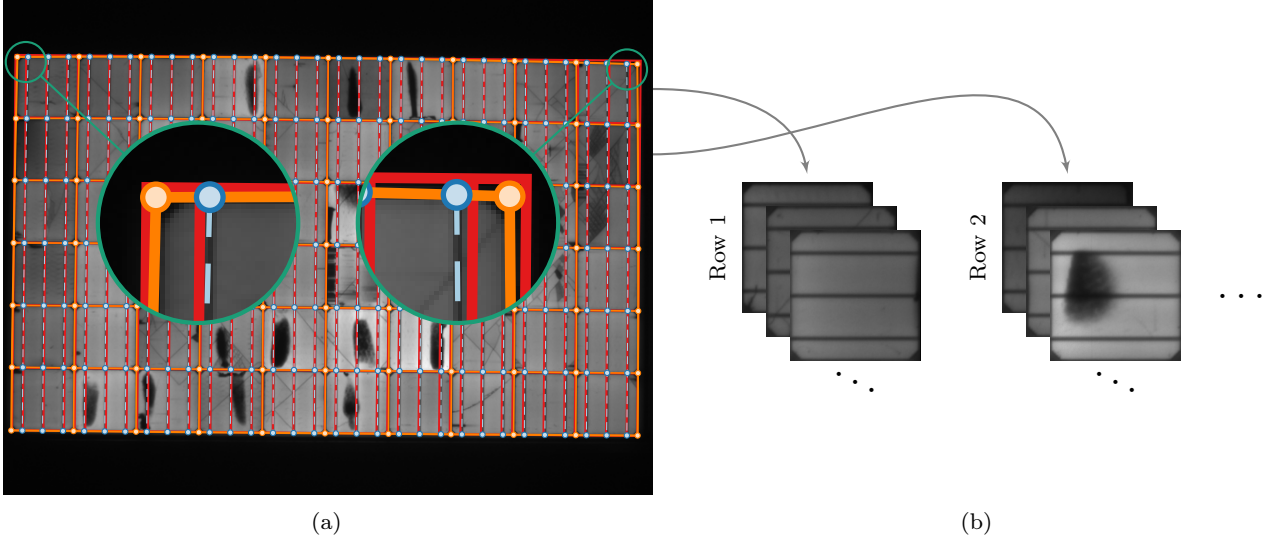


Figure 1: (a) An EL image of a PV module overlaid by a rectangular grid (—) and parabolic curve grid (—○—) including the busbars (—○—) determined using our approach. The intersections of the rectangular grid were registered to curve grid intersections to accurately align both grids. Notice how the rectangular grid is still not able to capture the curved surface of the solar module induced by the (weak) lens distortion that increases especially towards the image border. Using the curve grid, we estimate the lens distortion, rectify the image and finally extract the individual cells using the estimated module topology (b). The segmented solar cells can be used for further analysis, such as automatic defect classification or failure prediction in PV modules.

and with the shape of individual solar cell wafers. Also, cell cracks and other defects can introduce distracting streaks. A solar cell completely disconnected from the electrical circuit will also appear much darker than a functional cell. Additionally, solar modules vary in the number of solar cells and their layout, and solar cells themselves are oftentimes subdivided by busbars into multiple segments of different sizes. Therefore, it is desirable for a fully automated segmentation to infer both the arrangement of solar cells within the PV module and their subdivision from EL images alone, in a way that is robust to various disturbances. In particular, this may ease the inspection of heterogeneous batches of PV modules.

In this work, we assume that EL images are captured in a manufacturing setting. In this case, the EL irradiation of the solar module predominates the background irradiation, and the solar modules are captured facing the EL camera without major perspective distortion. Thus, the geometric distortions that are corrected by the proposed method are radial lens distortion, in-plane rotation, and minor perspective distortions. This distinguishes the manufacturing setting from acquisitions in the field, where PV modules may be occluded by cables and parts of the rack, and the perspective may be strong enough to require careful correction. However, perspective distortion also makes it more difficult to identify defective areas (*e.g.*, microcracks) due to

the foreshortening effect [2]. Therefore, capturing EL images from an extreme perspective is generally not sensible. Specifically for manufacturing environments, however, the proposed method yields a robust, highly accurate, and completely automatic segmentation of solar modules into solar cells from high resolution EL images of PV modules.

We hope that the proposed method facilitates new research to better understand the influence of module degradation on module efficiency and power generation. A robust segmentation of solar cells allows to continuously and automatically monitor the degradation process, for instance, by observing the differences in a series of solar cell images captured over a certain period of time. The segmentation also allows to automatically create training data for learning-based algorithms for defect classification and failure prediction.

1.1 Contributions

To the best of our knowledge, the proposed segmentation pipeline is the first work to enable a fully automatic extraction of solar cells from uncalibrated EL images of solar modules (*cf.*, Fig. 1b). It performs a highly accurate pixelwise classification into active solar cell area on monocrystalline and polycrystalline PV modules, and it is robust to various typical defects in solar modules. Within the segmentation pipeline, one par-

ticular contribution is a robust initialization with only few parameters for estimating lens distortion.

1.2 Outline

The remainder of this work is organized as follows. Section 2 discusses the related work. In Section 3, the individual stages of the segmentation pipeline are presented. In Section 4, we evaluate the presented segmentation approach on a number of different PV modules with respect to the segmentation accuracy. Finally, the conclusions are given in Section 5.

2 Related Work

The segmentation of PV modules into individual solar cells is related to the detection of calibration patterns, such as checkerboard patterns commonly used for calibrating intrinsic camera and lens parameters [66, 57, 23, 33, 28]. However, the appearance of calibration patterns is typically perfectly known, whereas detection of solar cells is encumbered by various defects that are a-priori unknown. Additionally, the number and layout of solar cells in PV modules is also assumed to be unknown. For the estimation of lens parameters, the lens distortion of EL images of PV modules may be too weak to apply existing approaches that rely on strong image deformations to unambiguously deduce the lens parameters.

To estimate the parameters of a lens distortion model, the plumbline constraint is typically employed [6]. The constraint exploits the fact that the projection of straight lines under radial and tangential distortion will not be truly straight. For example, under radial distortion, straight lines are captured as curves. For typical visual inspection tasks, a single image is sufficient to estimate the lens distortion parameters [14, 19, 11, 12, 65]. This can be achieved by decoupling the intrinsic parameters of the camera from the parameters of the lens distortion model.

Novel methodologies employ CNNs for various segmentation tasks. Existing CNN-based segmentation tasks can be categorized into (1) object detection, (2) semantic segmentation, and (3) instance-aware segmentation. One of the first CNN object detection architectures is Regions with CNN features (R-CNN) [25] to learn features that are subsequently classified using a class-specific linear Support Vector Machine (SVM) to generate region proposals. R-CNN learns to simultaneously classify object proposals and refine their spatial locations. The predicted regions, however, provide only a coarse estimation of object's location by means of

bounding boxes. Girshick [24] proposed Fast Region-based Convolutional Neural Network (Fast R-CNN) by accelerating training and testing times while also increasing the detection accuracy. Ren et al. [62] introduced Region Proposal Network (RPN) that shares full-image convolutional features with the detection network enabling nearly cost-free region proposals. RPN is combined with Fast R-CNN into a single network that simultaneously predicts object bounds and estimates the probability of an object for each proposal. For semantic segmentation, Long et al. [47] introduced Fully Convolutional Networks (FCNs) allowing for pixelwise inference. The FCN is learned end-to-end and pixels-to-pixels requiring appropriately labeled training data. Particularly, in medical imaging the U-Net network architecture by Ronneberger et al. [64] has been successfully applied for various segmentation tasks. In instance segmentation, Li et al. [42] combined segment proposal and object detection for Fully Convolutional Instance Segmentation (FCIS) where the general idea is to predict the locations in a fully convolutional network. He et al. [31] proposed a Mask R-CNN which extends Faster R-CNN.

The work by Mehta et al. [51] introduces a CNN for the prediction of power loss. Their system additionally localizes and classifies the type of soiling. Their work is based on RGB images of whole PV modules and addresses the additional geometric challenges of acquisitions in the field. In contrast, this work operates on EL images of individual cells of a PV module, and in particular focuses on their precise segmentation in a manufacturing setting.

The main limitation of learning-based approaches is the requirement of a considerable number of appropriately labeled images for training. However, pixelwise labeling is time-consuming, and in absence of data not possible at all. Also, such learning-based approaches require training data that is statistically representative for the test data, which oftentimes requires to re-train a model on data with different properties. In contrast, the proposed approach can be readily deployed to robustly segment EL images of PV modules without notable requirements of labeled training data.

The closest work related to the proposed method was presented by Sovetkin and Steland [69]. This method proposes a robust PV module grid alignment for the application on field EL images, where radial and perspective distortion, motion blur, and disturbing background may be present. The method uses an external checkerboard calibration for radial distortion correction, and prior knowledge on the solar cell topology in terms of the relative distances of the grid lines separating the busbars and cell segments. In contrast, EL images taken under manufacturing conditions may be

cropped or rotated, and the camera is not always pre-calibrated. Hence, the proposed method performs an automated on-line calibration for every EL image. This is particularly useful for EL images of PV modules from various sources, for which the camera parameters may not be available, or when zoom lenses are used. Additionally, the proposed method performs a pixelwise classification of pixels belonging to the active cell area and therefore is able to provide masks tailored to a specific module type. Such masks allow to exclude unwanted background information and to simplify further processing.

3 Methodology

The proposed framework uses a bottom-up pipeline to gradually infer a high-level representation of a solar module and its cells from low-level edge features in an EL image. Cell boundaries and busbars are represented as parabolic curves to robustly handle radial lens distortion which causes straight lines to appear curved in the image. Once we estimated the lens distortion parameters, the parabolas are rectified to obtain a planar cell grid. This rectified representation is used to segment the solar cells.

3.1 Overview

The general framework for segmenting the solar cells in EL images of PV modules is illustrated in Fig. 2 and consists of the following steps. First, we locate the busbars and the inter solar cell borders by extracting the ridge edges. The ridge edges are extracted at subpixel accuracy and approximated by a set of smooth curves defined as second-degree polynomials. The parametric representation is used to construct an initial grid of perpendicularly arranged curves that identify the PV module. Using this curve grid, we estimate the initial lens distortion parameters and hypothesize the optimal set of curves by further excluding outliers in a RANdom SAmple Consensus (RANSAC) scheme. Then we refine the lens distortion parameters that we eventually use to rectify the EL image. From the final set of curves we infer the PV module configuration and finally extract the size, perspective, and orientation of solar cells.

3.2 Preprocessing

First, the contrast of an EL image is stretched to the full range of intensity values. Then, low-level edge processing is applied to attenuate structural variations that might stem from cracks or silicon wafer texture, with the goal of preserving larger lines and curves.

3.2.1 Contrast Stretching

Here, we follow the approach by Franken et al. [22]. A copy I_{bg} of the input EL image I is blurred with a Gaussian kernel, and a morphological closing with a disk-shaped structure element is applied. Dividing each pixel of I by I_{bg} attenuates unwanted background noise while emphasizing high contrast regions. Then, histogram equalization [27, pp. 134 sqq.] is applied to increase its overall contrast. Figure 5b shows the resulting image I .

3.2.2 Gaussian Scale-Space Ridgeness

High-level grid structure of a PV module is defined by inter-cell borders and busbar which correspond to ridges in the image. Ridge edges can be determined from second-order partial derivatives summarized by a Hessian. To robustly extract line and curve ridges, we compute the second-order derivative of the image at multiple scales [45, 46]. The responses are computed in a Gaussian pyramid constructed from an input EL image [44]. This results in several layers of the pyramid at varying resolutions commonly referred to as octaves. The eigendecomposition of the Hessian computed afterwards provides information about line-like structures.

Let $\mathbf{u} := (u, v)^\top$ denote discrete pixel coordinates, $O \in \mathbb{N}$ the number of octaves in the pyramid, and $P \in \mathbb{N}$ the number of sublevels in each octave. At the finest resolution, we set σ to the golden ratio $\sigma = 1 + \sqrt{5}/2 \approx 1.6$. At each octave $o \in \{0, \dots, O-1\}$ and sublevel $\ell \in \{0, \dots, P-1\}$, we compute the Hessian by convolving the image with the derivatives of the Gaussian kernel. To obtain the eigenvalues, the symmetric Hessian is diagonalized by annihilating the off-diagonal elements using the Jacobi method which iteratively applies Givens rotations to the matrix [26]. This way, its eigenvalues and the corresponding eigenvectors can be simultaneously extracted in a numerically stable manner. Let $\mathbf{H} = \mathbf{V}\mathbf{\Lambda}\mathbf{V}^\top$ denote the eigendecomposition of the Hessian \mathbf{H} , where $\mathbf{\Lambda} := \text{diag}(\lambda_1, \lambda_2) \in \mathbb{R}^{2 \times 2}$ is a diagonal matrix of eigenvalues $\lambda_1 > \lambda_2$ and $\mathbf{V} := (\mathbf{v}_1, \mathbf{v}_2)$ are the associated eigenvectors. Under a Gaussian assumption, the leading eigenvector dominates the likelihood if the associated leading eigenvalue is spiked. In this sense, the local ridgeness describes the likelihood of a line segment in the image at position \mathbf{u} , and the orientation of the associated eigenvector specifies the complementary angle $\beta(\mathbf{u})$ of the most likely line segment orientation at position \mathbf{u} . The local ridgeness $R(\mathbf{u})$ is obtained as the maximum positive eigenvalue $\lambda_1(\mathbf{u})$ across all octaves and sublevels. Both the ridgeness $R(\mathbf{u})$

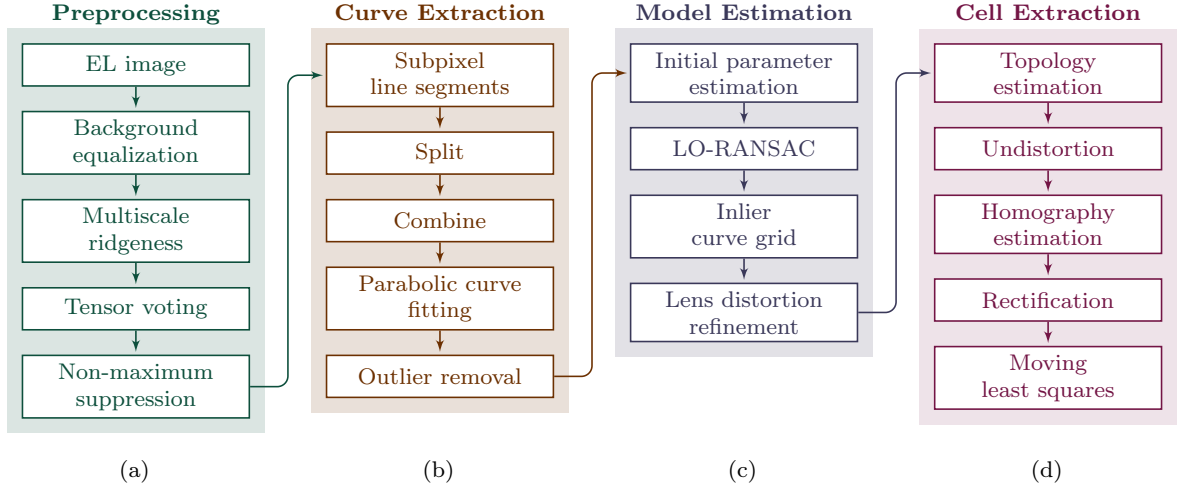


Figure 2: The proposed PV module segmentation pipeline consists of four stages. In the preprocessing stage (a), all contours are extracted. In the curve extraction stage (b), combinations of line segment are determined that fit to parabolic curves. In the model estimation stage (c), the lens distortion and inlier parabolic curves are determined. In the cell extraction stage (d) the cell topology is determined and the cells are extracted.

and the angle $\beta(\mathbf{u})$ provide initial cues for ridge edges in the EL image (see Fig. 5c).

3.2.3 Contextual Enhancement via Tensor Voting

Ridgeness can be very noisy (*cf.*, Fig. 5c). To discern noise and high curvatures from actual line and curve features, $R(\mathbf{u})$ is contextually enhanced using tensor voting [50].

Tensor voting uses a stick tensor voting field to model the likelihood that a feature in the neighborhood belongs to the same curve as the feature in the origin of the voting field [21]. The voting field is defined in terms of the likelihood function

$$w(\mathbf{x}) = \exp\left(-\frac{r^2}{2\varsigma^2} \cos^{2\nu} \phi\right) \quad (1)$$

that indicates whether $\mathbf{x} = (r \cos \phi, r \sin \phi)^\top$ for $0 \leq \phi \leq 2\pi$ given in polar coordinates passes through a curve, and $\gamma(\mathbf{x}) = 2\phi$ specifies the most likely angle of that curve. $\varsigma > 0$ controls the proximity of the voting field, and ν determines the angular specificity that we set to $\nu = 2$ in our experiments. w and γ are combined to generate a tensorial filter kernel $\mathbf{V}: \mathbb{R}^2 \rightarrow \mathbb{R}^{2 \times 2}$ that assigns a square matrix to all spatial positions as

$$\mathbf{V}(\mathbf{x}) = w(\mathbf{x}) \mathbf{c}(\mathbf{x}) \mathbf{c}(\mathbf{x})^\top \quad (2)$$

for $\mathbf{c}(\mathbf{x}) = (\cos \gamma(\mathbf{x}), \sin \gamma(\mathbf{x}))^\top$. The input is ridgeness R and orientation β , and the output is a tensor field

$$\mathbf{U}(\mathbf{x}) = \int_{\Omega} R(\mathbf{x}') \mathbf{V}^\beta(\mathbf{x}') (\mathbf{x} - \mathbf{x}') d\mathbf{x}' , \quad (3)$$

where $\Omega \subset \mathbb{R}^2$ denotes the image domain and $\mathbf{V}^\beta(\mathbf{x})$ the tensorial voting field rotated by a 2-D rotation matrix $\mathbf{R}_\beta \in \text{SO}(2)$ given by angle β [50],

$$\mathbf{V}^\beta(\mathbf{x}) = \mathbf{R}_\beta \mathbf{V}(\mathbf{R}_\beta^\top \mathbf{x}) \mathbf{R}_\beta^\top . \quad (4)$$

Following Franken et al. [21], stickness $\tilde{R}(\mathbf{u}) = \tilde{\lambda}_1 - \tilde{\lambda}_2$ is computed as the difference between the two eigenvalues $\tilde{\lambda}_1, \tilde{\lambda}_2$ of the tensor field \mathbf{U} , where $\tilde{\lambda}_1 > \tilde{\lambda}_2$. $\tilde{\beta}(\mathbf{u}) = \angle \tilde{\mathbf{e}}_1$ is the angle of the eigenvector $\tilde{\mathbf{e}}_1 \in \mathbb{R}^2$ associated with the largest eigenvalue $\tilde{\lambda}_1$, analogously to $\beta(\mathbf{u})$. Equation (3) can be efficiently computed as a sum of eight convolutions in the Fourier domain using steerable tensor voting. We iterate tensor voting two times, since one pass is not always sufficient [22]. Unlike Franken et al., however, we do not thin out the stickness immediately after the first pass to avoid too many disconnected edges. Given the high resolution of the EL images in our dataset of approximately 2500×2000 pixels, we use a fairly large proximity of $\varsigma_1 = 15$ in the first tensor voting step, and $\varsigma_2 = 10$ in the second. Figure 5d shows a typical stickness $\tilde{R}(\mathbf{u})$ output.

The stickness along the orientation $\tilde{\beta}(\mathbf{u})$ is used to extract curves at subpixel accuracy in the next step of the pipeline.

3.3 Curve Extraction

Centerline points of ridges are grouped by their curvature. Parabolic curves are fitted to these points, which yields a higher level representation, while simultaneously discarding point outliers.

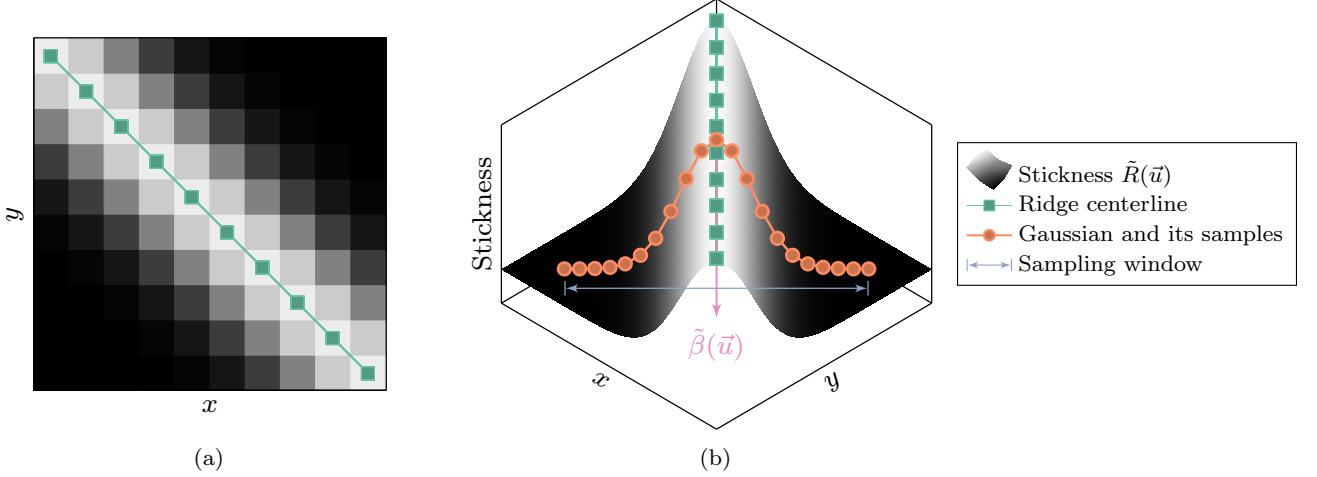


Figure 3: Extraction of ridge edges from stickness at subpixel accuracy. (a) shows a stickness patch with its initial centerline (—■—) at discrete coordinates obtained by skeletonization. The refined ridge centerline at subpixel accuracy is estimated by fitting a Gaussian function (—●—) to the cross-section profile of the ridge edge in (b) to equidistantly sampled stickness values within a predefined sampling window (—↔—).

3.3.1 Extraction of Ridges at Subpixel Accuracy

To ensure a high estimation accuracy of lens distortion parameters, we extract ridge edges at subpixel accuracy. This also makes the segmentation more resilient in out-of-focus scenarios, where images may appear blurry and the edges more difficult to identify due to smoother edge gradients.

To this end, we perform non-maximum suppression by Otsu’s global thresholding [55] on the stickness $\tilde{R}(\mathbf{u})$ followed by skeletonization [67]. Afterwards, we collect the points that represent the centerline of the ridges through edge linking [40]. These coarse positions can be refined by setting the centerline to the mean of a Gaussian function fitted to the edge profile [17] using the Gauss-Newton (GN) optimization algorithm [54]. The 1-dimensional window of the Gaussian is empirically set to 21 pixels, with four sample points per pixel that are computed via bilinear interpolation. The GN algorithm is initialized with the sample mean and standard deviation in the window, and multiplicatively scaled to the stickness magnitude at the mean. The mean of the fitted Gaussian is then reprojected along the edge profile oriented at $\tilde{\beta}(\mathbf{u})$ to obtain the edge subpixel position. Figure 3 visualizes these steps.

3.3.2 Connecting Larger Curve Segments

A limitation of the edge linking method is that it does not prioritize curve pairs with similar orientation. To address this, we first reduce the set of points that constitute a curve to a sparse representation using the non-parametric variant of the Ramer-Douglas-Peucker

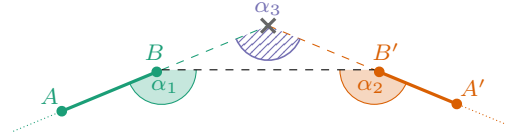


Figure 4: When considering combining two adjacent curve segments, one with the end line segment \overline{AB} and the other with the start line segment $\overline{B'A'}$, we evaluate the angles α_1 , α_2 , and α_3 and ensure they are below the predefined threshold ϑ with $\alpha_1, \alpha_2 \geq \alpha_3 \geq \pi - \vartheta$. This way, the combined curve segments are ensured to have a consistent curvature.

algorithm [61, 15] introduced by Prasad et al. [59]. Afterwards, edges are disconnected if the angle between the corresponding line segments is nonzero. In a second pass, two line segments are joined if they are nearby, of approximately the same length, and pointing into the same direction within an angle range $\vartheta = 5^\circ$. Figure 4 illustrates the way two curve segments are combined.

In the final step, the resulting n_i points of the i -th curve of a line segment form a matrix $\hat{\mathbf{Q}}^{(i)} \in \mathbb{R}^{2 \times n_i}$. For brevity, we denote the j -th column of $\hat{\mathbf{Q}}^{(i)}$ by $\hat{\mathbf{q}}_j \in \mathbb{R}^2$. $\hat{\mathbf{Q}}^{(i)}$ is used to find the parametric curve representation.

3.3.3 Parametric Curve Representation

Projected lines are represented as second-degree polynomials to model radial distortion. The curve parameters are computed via linear regression on the curve points.

More specifically, let

$$f(x) = a_2x^2 + a_1x + a_0 \quad (5)$$

denote a second-degree polynomial in horizontal or vertical direction. The curve is fitted to line segment points $\hat{\mathbf{q}}_j \in \{(x_j, y_j)^\top \mid j = 1, \dots, n_i\} \subseteq \hat{\mathbf{Q}}^{(i)}$ of the i -th curve $\hat{\mathbf{Q}}^{(i)}$ by minimizing the Mean Squared Error (MSE)

$$\text{MSE}(f) = \frac{1}{n_i} \sum_{j=1}^{n_i} (f(x_j) - y_j)^2 \quad (6)$$

using RANSAC iterations [18]. In one iteration, we randomly sample three points to fit Eq. (5), and then determine which of the remaining points support this curve model via MSE. Outlier points are discarded if the squared difference between the point and the parabolic curve value at its position exceeds $\rho = 1.5$. To keep the computational time low, RANSAC is limited to 100 iterations, and stopped early once sufficiently many inliers at a 99% confidence level are found [30, ch. 4.7]. After discarding the outliers, each curve is refitted to supporting candidate points using linear least squares [26]. To ensure a numerically stable and statistically robust fit, the 2-D coordinates are additionally normalized [29].

3.4 Curve Grid Model Estimation

The individual curves are used to jointly form a grid, which allows to further discard outliers, and to estimate lens distortion. To estimate the lens distortion, we employ the plumbline constraint [6]. The constraint models the assumption that curves in the image correspond to straight lines in real world. In this way, it becomes possible to estimate distortion efficiently from a single image, which allows to use this approach also post-hoc on cropped, zoomed or similarly processed images.

3.4.1 Representation of Lens Distortion

Analogously to Devernay and Faugeras [14], we represent the radial lens distortion by a function $L: \mathbb{R}_{\geq 0} \rightarrow \mathbb{R}_{\geq 0}$ that maps the distance of a pixel from the distortion center to a distortion factor. This factor can be used to radially displace each normalized image coordinate $\tilde{\mathbf{x}}$.

Image coordinates are normalized by scaling down coordinates $\mathbf{x} := (x, y)^\top$ horizontally by the distortion aspect ratio s_x (corresponding to image aspect ratio decoupled from the projection on the image plane) followed by shifting the center of distortion $\mathbf{c} := (c_x, c_y)^\top$ to the origin and normalizing the resulting 2-D point to

the unit range using the dimensions $M \times N$ of the image of width M and height N . Homogeneous coordinates allow to express the normalization conveniently using a matrix product. By defining the upper-triangular matrix

$$\mathbf{K} = \begin{bmatrix} s_x M & 0 & c_x \\ 0 & N & c_y \\ 0 & 0 & 1 \end{bmatrix} \quad (7)$$

the normalizing mapping $\mathbf{n}: \Omega \rightarrow [-1, 1]^2$ is

$$\mathbf{n}(\mathbf{x}) = \boldsymbol{\pi} (\mathbf{K}^{-1} \boldsymbol{\pi}^{-1}(\mathbf{x})) \quad , \quad (8)$$

where $\boldsymbol{\pi}: \mathbb{R}^3 \rightarrow \mathbb{R}^2$ projects homogeneous to inhomogeneous coordinates,

$$\boldsymbol{\pi}: (x, y, z)^\top \mapsto \frac{1}{z}(x, y)^\top, \quad \text{for } z \neq 0 \quad (9)$$

and the inverse operation $\boldsymbol{\pi}^{-1}: \mathbb{R}^2 \rightarrow \mathbb{R}^3$ backprojects inhomogeneous to homogeneous coordinates:

$$\boldsymbol{\pi}^{-1}: (x, y)^\top \mapsto (x, y, 1)^\top \quad . \quad (10)$$

Note that the inverse mapping \mathbf{n}^{-1} converts normalized image coordinates to image plane coordinates.

3.4.2 The Field-of-View Lens Distortion Model

To describe the radial lens distortion, we use the first-order Field-of-View (FOV) lens model by Devernay and Faugeras that has a single distortion parameter ω . While images can also suffer from tangential distortion, this type of distortion is often negligible [75]. The sole parameter $0 < \omega \leq \pi$ denotes the opening angle of the lens. The corresponding radial displacement function L is defined in terms of the distortion radius $r \geq 0$ as

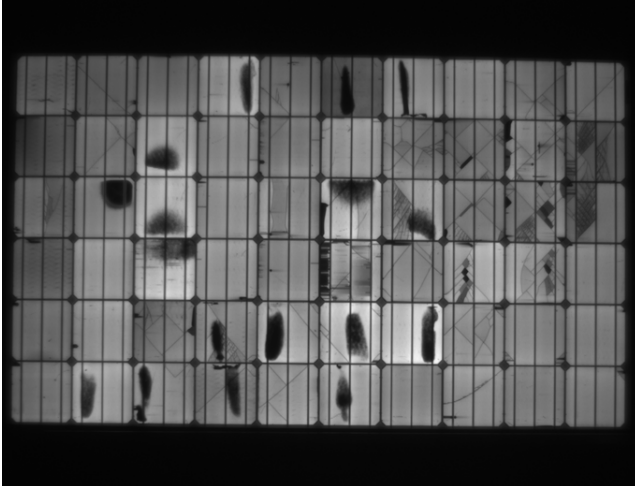
$$L(r) = \frac{1}{\omega} \arctan \left(2r \tan \frac{\omega}{2} \right) \quad , \quad \text{for } \omega \neq 0 \quad . \quad (11)$$

One advantage of the model is that its inversion has a closed-form solution with respect to the distortion radius r .

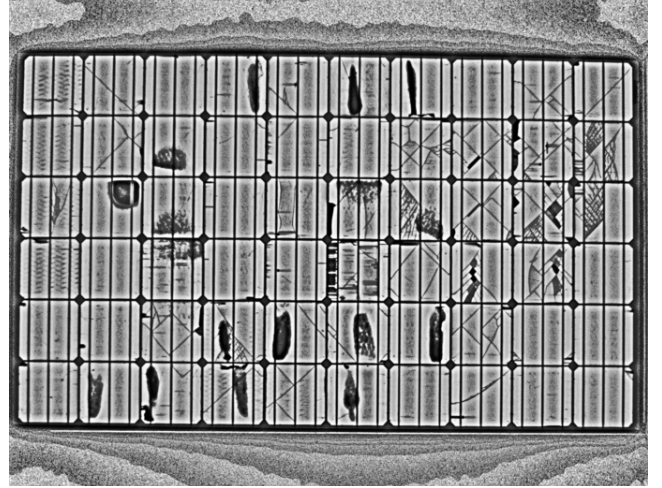
Similar to Devernay and Faugeras, we decouple the distortion from the projection onto the image plane, avoiding the need to calibrate for intrinsic camera parameters. Instead, the distortion parameter ω is combined with the distortion center $\mathbf{c} \in \Omega$ and distortion aspect ratio s_x which are collected in a vector $\boldsymbol{\theta} := (\mathbf{c}, s_x, \omega)$.

Normalized undistorted image coordinates $\tilde{\mathbf{x}}_u = \boldsymbol{\delta}^{-1}(\tilde{\mathbf{x}}_d)$ can be directly computed from distorted coordinates $\tilde{\mathbf{x}}_d$ as

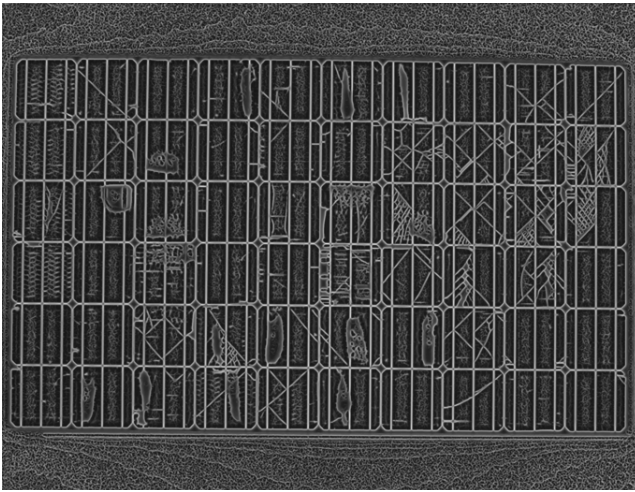
$$\boldsymbol{\delta}^{-1}(\tilde{\mathbf{x}}_d) = \frac{L^{-1}(r_d)}{r_d} \tilde{\mathbf{x}}_d \quad , \quad \text{for } r_d \neq 0 \quad (12)$$



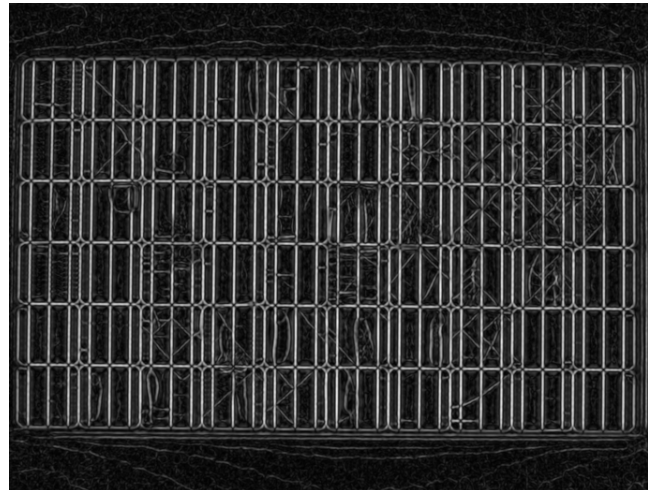
(a) EL image of a monocrystalline PV module



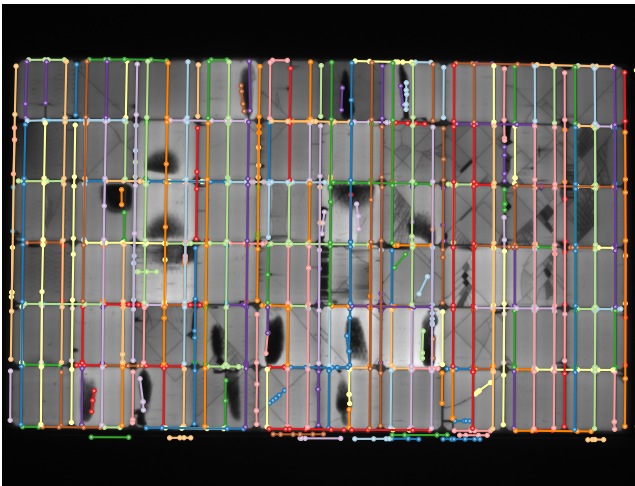
(b) Background-equalized image



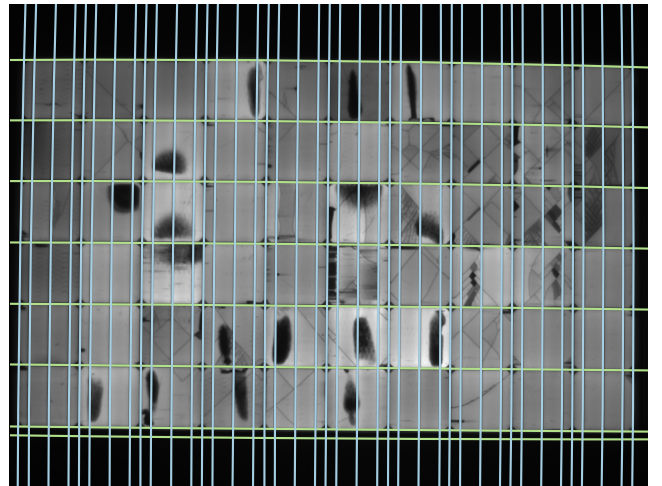
(c) Ridgeness image $R(\mathbf{u})$ from the filter responses at multiple scales



(d) Stickness of ridgeness contextually enhanced using tensor voting



(e) Extracted line segments grouped by their curvature



(f) Horizontal (red) and vertical (blue) parabolic curves filtered using the intersection constraint

Figure 5: Visualization of the preprocessing, curve extraction, and model estimation stages for the PV module from Fig. 1

where $r_d = \|\tilde{\mathbf{x}}_d\|_2$ is the distance of $\tilde{\mathbf{x}}_d$ from the origin. $L^{-1}(r)$ is the inverse of the lens distortion function in Eq. (11), namely

$$L^{-1}(r) = \frac{\tan r\omega}{2 \tan \frac{\omega}{2}}, \quad \text{for } \omega \neq 0. \quad (13)$$

The function that undistorts a point $\mathbf{x} \in \Omega$ is thus

$$\mathbf{u}(\mathbf{x}) = \mathbf{n}^{-1}(\delta^{-1}(\mathbf{n}(\mathbf{x}))) \quad (14)$$

Note that Eq. (12) exhibits a singularity at $r_d \approx 0$ for points close to the distortion center. By inspecting the function's limits, one obtains

$$\lim_{r_d \rightarrow 0^+} \delta^{-1}(\tilde{\mathbf{x}}_d) = \frac{\omega}{2 \tan \frac{\omega}{2}} \tilde{\mathbf{x}}_d. \quad (15)$$

Analogously, Eq. (13) is singular at $\omega = 0$ but approaches $\lim_{r \rightarrow 0^+} L^{-1}(r) = r$ at the limit. In this case, Eq. (12) is an identity transformation which does not radially displace points.

3.4.3 Estimation of Initial Lens Distortion Model Parameters

Lens distortion is specified by the distortion coefficient ω , the distortion aspect ratio s_x , and the distortion center \mathbf{c} . Naive solution leads to a non-convex objective function with several local minima. Therefore, we first seek an initial set of parameters close to the optimum, and then proceed using a convex optimization to refine the parameters.

We initialize the distortion aspect ratio to $s_x = 1$, and the distortion center to the intersection of two perpendicular curves with smallest coefficients in the highest order polynomial term. Such curves can be assumed to have the smallest curvature and are thus located near the distortion center.

To find the intersection of two perpendicular curves, we denote the coefficients of a horizontal curve by a_2, a_1, a_0 , and the coefficients of a vertical curve by b_2, b_1, b_0 . The position x of a curve intersection is then the solution to

$$a_2^2 b_2 x^4 + 2a_1 a_2 b_2 x^3 + x^2 (2a_0 a_2 b_2 + a_1^2 b_2 + a_2 b_1) + x \cdot (2a_0 a_1 b_2 + a_1 b_1 - 1) + a_0^2 b_2 + a_0 b_1 + b_0 = 0. \quad (16)$$

The real roots of the quartic (16) can be found with the Jenkins-Traub RPOLY algorithm [37] or a specialized quartic solver [20]. The corresponding values $f(x)$ are determined by inserting the roots back into Eq. (5).

Distortion Coefficient Estimation of the distortion coefficient ω from a set of distorted image points is not straightforward because the distortion function $L(r)$ is non-linear. One way to overcome this problem is to linearize $L(r)$ with Taylor polynomials, and to estimate ω with linear least squares.

To this end, we define the distortion factor

$$k := \frac{L(r)}{r}, \quad \text{for } k \in \mathbb{R}_{>0} \quad (17)$$

which maps undistorted image points $\{\mathbf{p}_j\}_{j=1}^n$ lying on the straight lines to distorted image points $\{\mathbf{q}_j\}_{j=1}^n$ lying on the parabolic curves. Both point sets are then related by

$$\mathbf{p}k = \mathbf{q}. \quad (18)$$

The distorted points \mathbf{q}_j are straightforward to extract by evaluating the second-degree polynomial of the parabolic curves. To determine \mathbf{p}_j , we define a line with the first and the last point in \mathbf{q}_j , and select points from this line. Collecting these points in the vectors $\mathbf{p} \in \mathbb{R}^{2n}$ and $\mathbf{q} \in \mathbb{R}^{2n}$ yields an overdetermined system of $2n$ linear equations in one unknown. \hat{k} is then estimated via linear least squares as

$$\hat{k} = \underset{k}{\operatorname{argmin}} \|\mathbf{q} - \mathbf{p}k\|_2^2, \quad (19)$$

where the solution is found via the normal equations [26] as

$$\hat{k} := \frac{\mathbf{p}^\top \mathbf{q}}{\mathbf{p}^\top \mathbf{p}}. \quad (20)$$

The points $\mathbf{q}_j, \mathbf{p}_j$ refer to the columns of the two matrices $\mathbf{Q}^{(i)}, \mathbf{P}^{(i)} \in \mathbb{R}^{2 \times n_i}$, respectively, where n_i again denotes the number of points, which are used in the following step of the pipeline.

To determine ω from the relation $k = \frac{L(r)}{r}$, $L(r)$ is expanded around $\omega_0 = 0$ using Taylor series. More specifically, we use a second-order Taylor expansion to approximate

$$\arctan(x) = x + \mathcal{O}(x^2), \quad (21)$$

and a sixth-order Taylor expansion to approximate

$$\tan(y) = y + \frac{y^3}{3} + \frac{2y^5}{15} + \mathcal{O}(y^6). \quad (22)$$

Let $L(r) = \frac{1}{\omega} \arctan(x)$ with $x = 2r \tan(y)$, and $y = \frac{\omega}{2}$. We substitute the Taylor polynomials from Eqs. (21) and (22), and x, y into Eq. (17) to obtain a biquadratic polynomial $Q(\omega)$ independent of r :

$$\frac{L(r)}{r} \approx 1 + \underbrace{\frac{1}{12}\omega^2 + \frac{1}{120}\omega^4}_{=: Q(\omega)}. \quad (23)$$

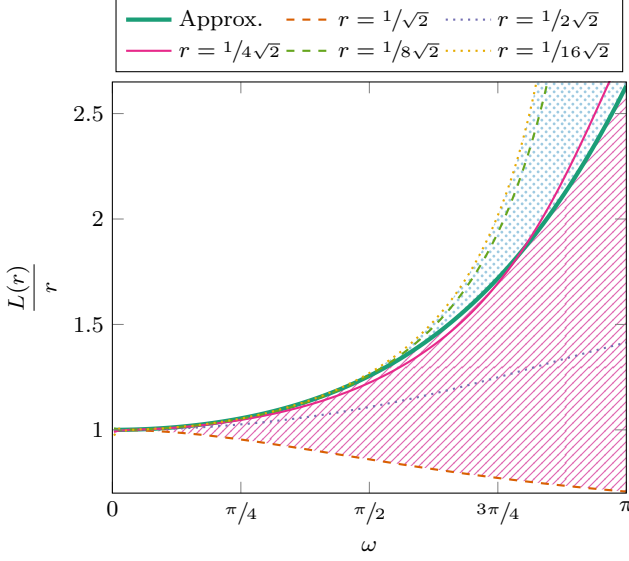


Figure 6: Approximation of the distortion coefficient ω using Eq. (23) (—) compared to the exact solution with respect to varying radii r . For large radii outside the range of normalized coordinates (*i.e.*, the radius of the half-unit circle $r > 1/\sqrt{2}$), the estimate is not accurate. This implies that the ideal sampled points must be both at some distance from the image border and also from the distortion center. As a side note, the estimation error becomes unacceptable for wide lenses where $\omega > \pi/4$. However, the EL images in this work are well below this threshold.

By equating the right-hand side of Eq. (23) to k

$$Q(\omega) = k \quad (24)$$

we can estimate ω from four roots of the resulting polynomial $Q(\omega)$. These roots can be found by substituting $z = \omega^2$ into Eq. (23), solving the quadratic equation with respect to z , and substituting back to obtain ω . This eventually results in the four solutions $\pm\sqrt{z_{1,2}}$. The solution exists only if $k \geq 1$, as complex solutions are not meaningful, and thus corresponds to the largest positive real root.

We evaluated the accuracy of the approximation (23) with the results shown in Fig. 6. For large radii, the approximation significantly deviates from the exact solution. In practice, this means that the selected points for the estimation must ideally be well distributed across the image. Otherwise, the lens distortion parameter will be underestimated. Note that this constraint is typically not an issue due to the spatial distribution of the solar cells across the captured EL image.

3.4.4 Minimization Criterion for the Refinement of Lens Distortion Parameters

The Levenberg-Marquardt algorithm [41, 48] is used to refine the estimated lens distortion parameters θ . The objective function is

$$\theta^* := \underset{\theta}{\operatorname{argmin}} \frac{1}{2} \sum_{i=1}^n \chi^2(\mathbf{P}^{(i)}, \theta) . \quad (25)$$

Here, $\mathbf{P}^{(i)} \in \mathbb{R}^{2 \times m}$ is a matrix of m 2-D points of the i -th curve. The distortion error χ^2 quantifies the deviation of the points from the corresponding ideal straight line by

$$\chi^2(\mathbf{P}^{(i)}, \theta) = t_1 \sin^2 \varphi - 2|t_2| |\sin \varphi| \cos \varphi + t_3 \cos^2 \varphi , \quad (26)$$

where

$$|\sin \varphi| = \sqrt{\frac{1}{2} - \alpha}, \quad \cos \varphi = \sqrt{\frac{1}{2} + \alpha} \quad (27)$$

with

$$\alpha = \frac{t_1 - t_2}{2\sqrt{(t_1 - t_2)^2 + 4t_2^2}} \quad (28)$$

and the coefficients t_1, t_2, t_3 are

$$t_1 = \sum_{j=1}^m x_j^2 - \frac{1}{m} \left(\sum_{j=1}^m x_j \right)^2 \quad (29)$$

$$t_2 = \sum_{j=1}^m x_j y_j - \frac{1}{m} \left(\sum_{j=1}^m x_j \right) \left(\sum_{j=1}^m y_j \right) \quad (30)$$

$$t_3 = \sum_{j=1}^m y_j^2 - \frac{1}{m} \left(\sum_{j=1}^m y_j \right)^2 . \quad (31)$$

The undistorted image coordinates $\mathbf{p}_j := (x_j, y_j)^\top \in \Omega$ are computed as $\mathbf{p}_j = \mathbf{u}(\mathbf{q}_j)$ by applying the inverse lens distortion given in Eq. (14) to the points \mathbf{q}_j of the i -th curve $\mathbf{Q}^{(i)}$. In a similar manner, the obtained points \mathbf{p}_j form the columns of a matrix $\mathbf{P}^{(i)} \in \mathbb{R}^{2 \times n_i}$.

Following [Devernay and Faugeras](#), we iteratively optimize the set of lens parameters θ . In every step t , we refine these parameters and then compute the overall error $\epsilon_t := \sum_{i=1}^n \chi^2(\mathbf{P}^{(i)}, \theta)$ using Eq. (26) over all curve points. Afterwards, we undistort the curve points and continue the optimization until the relative change in error $\epsilon := (\epsilon_{t-1} - \epsilon_t)/\epsilon_t$ falls below the threshold $\epsilon = 10^{-6}$.

Minimizing the objective function (26) for all parameters simultaneously may cause the optimizer to be trapped in a local minimum. We therefore optimize a subset of parameters in several partitions starting with ω only. Afterwards, we additionally optimize the distortion center \mathbf{c} . Finally, the parameters θ are jointly optimized.

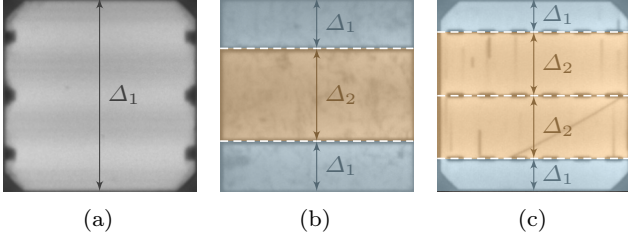


Figure 7: Estimation of solar module topology requires determining the number of subdivisions (*i.e.*, rectangular segments) in a solar cell. Common configurations include no subdivisions at all (*i.e.*, one segment) (a), three segments (b) and four segments (c). Notice how the arrangement of rectangular segments is symmetric and segment sizes increase monotonically towards the center, *i.e.*, $\Delta_1 < \dots < \Delta_n$. In particular, shape symmetry can be observed not only along the vertical axis of the solar cell but also along the horizontal one as well.

3.4.5 Obtaining a Consistent Parabolic Curve Grid Model

The layout of the curves is constrained to a grid in order to eliminate outlier curves. Ideally, each horizontally oriented parabola should intersect each vertically oriented parabola exactly once. This intersection can be found using Eq. (16). Also, every parabolic curve should not intersect other parabolic curves of same orientation within the image plane. This set of rules eliminates most of the outliers.

Robust Outlier Elimination Locally Optimized Random Sample Consensus (LO-RANSAC) [10] is used to remove outlier curves. In every LO-RANSAC iteration, the grid constraints are imposed by randomly selecting two horizontal and two vertical curves to build a minimal grid model. Inliers are all curves that (1) exactly once intersect the model grid lines of perpendicular orientation, (2) not intersect the model grid lines of parallel orientation, and (3) whose MSE of the reprojected undistorted points is not larger than one pixel.

Remaining Curve Outliers Halos around the solar modules and holding mounts (such as in Fig. 5) can generate additional curves outside of the cells. We apply Otsu’s thresholding [55] on the contrast-normalized image and discard outer curves that generate additional grid rows or columns with an average intensity in the enclosed region below the automatically determined threshold.

3.5 Estimation of the Solar Module Topology

A topology constraint on the solar cell can be employed to eliminate remaining non-cell curves in the background of the PV module, and the number and layout of solar cells can be subsequently estimated. However, outliers prevent a direct estimation of the number of solar cell rows and columns in a PV module. Additionally, the number and orientation of segments dividing each solar cell are generally unknown. Given the aspect ratio of solar cells in the imaged PV module, the topology can be inferred from the distribution of parabolic curves. For instance, in PV modules with equally long horizontal and vertical cell boundary lines, the solar cells have a square (*i.e.*, 1 : 1) aspect ratio.

The number of curves crossing each square image area of solar cell is constant. Clustering the distances between the curves allows to deduce the number of subdivisions within solar cells.

3.5.1 Estimation of the Solar Cell Subdivisions and the Number of Rows and Columns

The solar cells and their layout are inferred from the statistics of the line segment lengths in horizontal and vertical direction. We collect these lengths separately for each dimension and cluster them. DBSCAN clustering [16] is used to simultaneously estimate cluster membership and the number of clusters. Despite the presence of outlier curves, clusters are representative of the distribution of segment dimensions within a cell. For example, if a solar cell consists of three vertically arranged segments (as in Fig. 7b) with heights of 20 : 60 : 20 pixels, the two largest clusters will have the medians 60 and 20. With the assumption that the segment arrangement is typically symmetric, the number of segments is estimated as the number of clusters times two minus one. If clustering yields a single cluster, we assume that the solar cells consist of a single segment. Outlier curves or segments, respectively, are rejected by only considering the largest clusters, with the additional constraint that the sizes of the used clusters are proportional to each other, and that not more than two different segments (as in Fig. 7c) can be expected in a cell. The number of rows and columns of a solar cell is determined by dividing the overall size of the curve grid by the estimated cell side lengths.

3.5.2 Curve Grid Outlier Elimination

The estimated proportions are used to generate a synthetic planar grid that is registered against the curve grid intersections. Specifically, we use the rigid point set registration of Coherent Point Drift (CPD) [52].

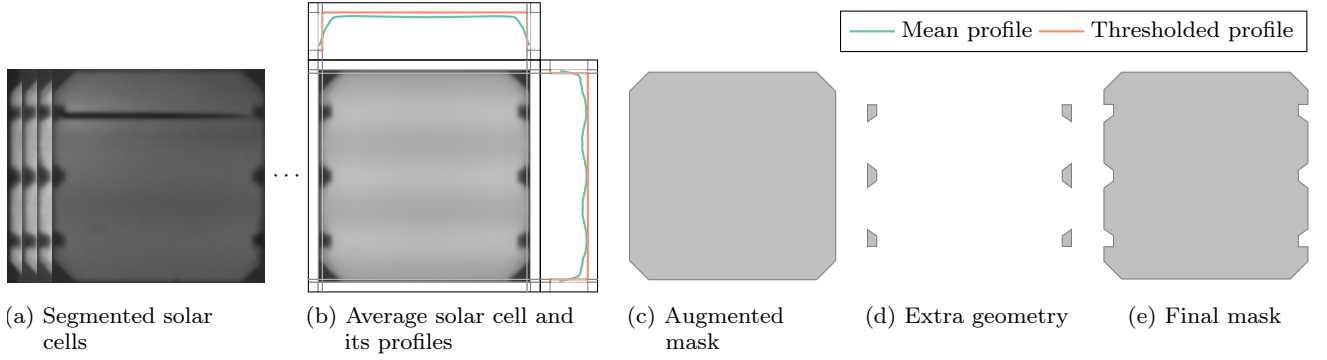


Figure 8: Intermediate steps of the solar mask estimation process

The method requires choosing a weight $0 \leq w \leq 1$ of the uniform distribution that accounts for noise and outliers, which we estimate as the proportion of points in the synthetic planar grid and the total number of intersections in the curve grid.

To ensure CPD convergence, initial positions of the synthetic planar grid should be sufficiently close to the curve grid intersections. We therefore estimate the translation and rotation of the planar grid to closely pre-align it with the grid we are registering against. The initial translation can be estimated as the curve grid intersection point closest to the image plane origin. The 2-D in-plane rotation is estimated from the average differences of two consecutive intersection points along each curve grid row and column. This results in two 2-D vectors which are approximately orthogonal to each other. The 2-D vector with the larger absolute angle is rotated by 90° such that both vectors become roughly parallel. The estimated rotation is finally obtained as the average angle of both vectors.

3.5.3 Undistortion and Rectification

The PV module configuration is used to undistort the whole image using Eq. (14). After eliminating the lens distortion, we use Direct Linear Transform (DLT) [30] to estimate the planar 2-D homography using the four corners of the curve grid with respect to the corners of the synthetic planar grid.

The intersections of the undistorted curve grid may not align exactly with respect to the synthetic planar grid. The remaining misalignment is therefore corrected via affine moving least squares [68], which warps the image using the planar grid intersections as control points distorted using the estimated lens parameters, and curve grid intersections are used as their target positions.

3.6 Estimation of the Active Solar Cell Area

We use solar cell images extracted from individual PV modules to generate a mask that represents the active solar cell area. Such masks allow to exclude the background and the busbars of a solar cell (see Fig. 8). In particular, active cell area masks are useful for detection of cell cracks since they allow to mask out the busbars, which can be incorrectly identified as cell cracks due to high similarity of their appearance [70, 72].

Estimation of solar cell masks is related to the image labeling problem, where the goal is to classify every pixel into several predefined classes (in our case, the background and the active cell area). Existing approaches solve this problem using probabilistic graphical models, such as a Conditional Random Field (CRF) which learns the mapping in a supervised manner through contextual information [32]. However, since the estimated curve grid already provides a global context, we tackle the pixelwise classification as a combination of adaptive thresholding and prior knowledge with regard to the straight shape of solar cells. Compared to CRFs, this approach does not require a training step and is easy to implement.

To this end, we use solar cells extracted from a PV module to compute a mean solar cell (see Figs. 8a to 8b). We then apply locally adaptive thresholding [56] on 25×25 pixels patches using their mean intensity, followed by a 15×15 morphological opening and flood filling to close any remaining holes. This leads to an initial binary mask.

Ragged edges at the contour are removed using vertical and horizontal cell profiles (Fig. 8b). The profiles are computed as pixelwise median of the initial mask along each image row or column, respectively. We combine the backprojection of these profiles with the convex hull of the binary mask determined with the method of Barber et al. [4] to account for cut-off edges using bitwise AND (*cf.*, Fig. 8c). To further exclude repetitive patterns in the EL image of a solar cell, *e.g.*, due to low

passivation efficiency in the contact region (see Fig. 8d), we combine the initial binary mask and the augmented mask via bitwise XOR.

We note that solar cells are usually symmetric about both axes. Thus, the active solar cell area mask estimation can be restricted to only on quadrant of the average solar cell image to enforce mask symmetry. Additionally, the convex hull of the solar cell and its extra geometry can be approximated by polygons [1] for a more compact representation.

3.7 Parameter Selection

The proposed solar cell segmentation pipeline relies on a set of parameters that directly affect the segmentation robustness and accuracy. Table 1 provides an overview of all parameters with their values used in this work.

Generally, the parameters depend on the setup used for EL image acquisition. The provided parameter values were found to work reliably especially for high resolution EL images and standard camera lenses, as in our dataset (*cf.*, Section 4.1). For low resolution EL images, however, the number of pyramid octaves and sublevels will need to be increased, to avoid missing important image details. Whereas, tensor voting proximity parameters, on contrary, will need to be lowered, since the width of ridge edges in low resolution images tends to be proportional to the image resolution. This immediately affects the size of the 1-D sampling window for determining the Gaussian-based subpixel position of curve points.

Curve extraction parameters correlate mainly with the field-of-view of the EL camera lens. In particular for wide angle lenses, the merge angle ϑ must be chosen accordingly by increasing the value.

Parabolic curve fit error ρ balances between robustness and accuracy of the segmentation result. The window size for locally adaptive thresholding used for estimation of solar cell masks correlates both with the resolution of EL images, but also with the amount of noise and texture variety in solar cells, *e.g.*, due to cell cracks.

4 Evaluation

We evaluate the robustness and accuracy of our approach against manually annotated ground truth masks. Further, we compare the proposed approach against the method by Sovetkin and Steland [69] on simplified masks, provide qualitative results and runtimes, and discuss limitations.

4.1 Dataset

We use a dataset consisting of 44 unique PV modules with various degrees of defects to manually select the parameters for the segmentation pipeline. In this dataset, 26 solar modules are of monocrystalline type, and 18 of polycrystalline type. The 44 solar modules consist in total of 2,624 solar cells of which 715 are definitely defective with defects ranging from microcracks to completely disconnected cells and mechanically induced cracks (*e.g.*, electrically insulated or conducting cracks, or cell cracks due to soldering [71]). 106 solar cells exhibit smaller defects that are not with certainty identifiable as completely defective, and 295 solar cells feature miscellaneous surface abnormalities that are no defects. The remaining 1,508 solar cells are categorized as functional without any perceivable surface abnormalities. The solar cells in imaged PV modules have a square aspect ratio (*i.e.*, are quadratic).

The average resolution of the EL images is $2,779.63 \times 2,087.35$ pixels with a standard deviation of image width and height of 576.42 and 198.30 pixels, respectively. The median resolution is $3,152 \times 2,046$ pixels.

Additional eight test EL images are used to carry out the evaluation. Four modules are monocrystalline and the remaining four are polycrystalline. Their ground truth segmentation masks consist of hand-labeled solar cell segments. The ground truth additionally specifies both the rows and columns of the solar cells, and their subdivisions. These images show various PV modules with a total of 408 solar cells. The resolution of the test EL images varies around $2,649.50 \pm 643.20 \times 2,074 \pm 339.12$ with a median image resolution of $2,581.50 \times 2,046$.

Three out of four monocrystalline modules consist of 4×9 cells and the remaining monocrystalline module consists of 6×10 cells. All of their cells are subdivided by busbars into 3×1 segments.

The polycrystalline modules consist of 6×10 solar cells each. In two of the modules, every cell is subdivided into 3×1 segments. The cells of the other two modules are subdivided into 4×1 segments.

4.2 Evaluation Metrics

We use two different metrics, pixelwise scores and the weighted Jaccard index to evaluate both the robustness and the accuracy of the proposed method and to compare our method against related work. In the latter case, we additionally use a third metric, the Root Mean Square Error (RMSE), to compute the segmentation error on simplified masks.

4.2.1 Root Mean Square Error

The first performance metric is the RMSE given in pixels between the corners of the quadrilateral mask computed from the ground truth annotations and the corners estimated by the individual modalities. The metric provides a summary of the method’s accuracy in absolute terms across all experiments.

4.2.2 Pixelwise Classification

The second set of performance metrics are precision, recall, and the F_1 score [63]. These metrics are computed by considering cell segmentation as a binary pixelwise classification into active cell area and background pixels. A correctly segmented active area pixel is a true positive, the remaining quantities are defined accordingly. It is worth mentioning that these metrics do not explicitly penalize mismatches between major segmentation errors. For example, if a segmentation merges two separate cells into one, pixels from both solar cells are counted as true positives. Yet only pixels corresponding to the background between these cells are considered as false negatives instead of the whole segment that was merged incorrectly.

4.2.3 Weighted Jaccard Index

The third performance metric is the weighted Jaccard index [9, 35], a variant of the metric widely known as Intersection-over-Union (IoU). This metric extends the common Jaccard index by an importance weighting of the input pixels. As the compared masks are not strictly binary either due to antialiasing or interpolation during mask construction, we define importance of pixels by their intensity. Given two non-binary masks A and B ,

the weighted Jaccard similarity is

$$J_w = \frac{\sum_{\mathbf{u} \in \Omega} \min\{A(\mathbf{u}), B(\mathbf{u})\}}{\sum_{\mathbf{u} \in \Omega} \max\{A(\mathbf{u}), B(\mathbf{u})\}}. \quad (32)$$

The performance metric is computed on pairs of segmented cells and ground truth masks. A ground truth cell mask is matched to the segmented cell with the largest intersection area, thus taking structural coherence into account.

We additionally compute the Jaccard index of the background, which corresponds to the accuracy of the method to segment the whole solar module. Solar cell misalignment or missed cells will therefore penalize the segmentation accuracy to a high degree. Therefore, the solar module Jaccard index provides a summary of how well the segmentation performs per EL image.

4.3 Quantitative Results

We evaluate the segmentation accuracy of our approach on a fixed set of parameters as specified in Table 1.

4.3.1 Comparison to Related Work with Simplified Cell Masks

The method by [Sovetkin and Steland](#) focuses on the estimation of the perspective transformation of the solar module and the extraction of solar cells. Radial distortion is corrected with a lens model of an external checkerboard calibration. The grid structure is fitted using a priori knowledge of the module topology. For this reason, we refer to the method as Perspective-corrected Grid Alignment (PGA). The method makes no specific proposal for mask generation and therefore yields rectangular solar cells.

In order to perform a comparison, the exact masks (*cf.*, Fig. 9a) are restricted to quadrilateral shapes (*cf.*,

Table 1: Overview of segmentation pipeline parameters and their values used in this work

§	Symbol	Description	Used value
3.2.2	O	Number of octaves in Gaussian scale-space pyramid	5
	P	Number of sublevels in each octave	8
	σ	Gaussian scale-space standard deviation	1.6
	γ	Gaussian scale-space pyramid downsampling factor	2
3.2.3	ν	Tensor voting angular specificity	2
	$\varsigma_{1,2}$	Proximity of the 1 st and 2 nd tensor voting steps	15, 10
3.3.1		1-D sampling window for Gaussian-based subpixel position	21
3.3.2	ϑ	Maximum merge angle of two neighboring line segments	5°
3.3.3	ρ	Maximum error between fitted parabolic curve value at curve point	1.5
3.4.4	ϵ	Minimal change in error during refinement of lens distortion parameters	10 ^{−6}
3.5		Solar cell aspect ratio	1 : 1
3.6		Locally adaptive thresholding window size	25 × 25

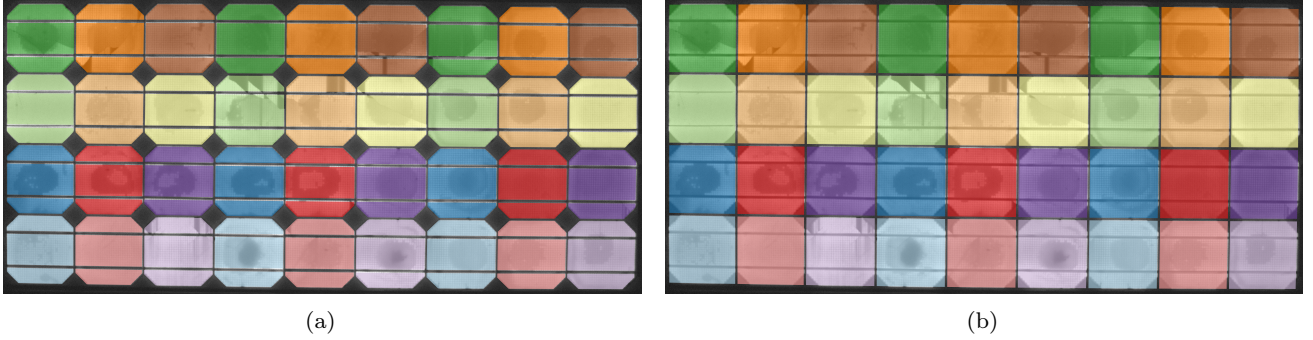


Figure 9: Example of an exact mask (a) of solar cells estimated using the proposed approach and a quadrilateral mask (b) determined from the exact mask. The latter is used for comparison against the method of Sovetkin and Steland [69]. Both masks are shown as color overlays. Different colors denote different instances of solar cells.

Table 2: Root Mean Square Error (RMSE), in pixels, of the distance between the corners of the quadrilateral mask determined from the ground truth annotations and the corners determined by the respective method in all eight test images. Bold face denotes smallest error.

	PGA		Proposed
	distorted	undistorted	
Monocrystalline	6.09	4.00	2.61
Polycrystalline	5.32	2.76	1.77
Overall	5.65	3.32	2.15

Fig. 9b). The quadrilateral mask is computed as the minimum circumscribing polygon with four sides, *i.e.*, a quadrilateral, using the approach of Aggarwal et al. [1]. The quadrilateral exactly circumscribes the convex hull of the solar cell mask with all the quadrilateral sides flush to the convex hull.

PGA assumes that radial distortion is corrected by an external checkerboard calibration. This can be a limiting factor in practice. Hence, the comparison below considers both practical situations by running PGA on distorted images and on undistorted images using the distortion correction of this work.

Root Mean Square Error Table 2 provides the RMSE in pixels between the corners of the quadrilaterals computed by the respective modality and the quadrilateral mask estimated from the ground truth. The metric is provided for monocrystalline and polycrystalline solar wafers separately, and for both types combined. In all cases, the proposed approach outperforms both PGA variants. We particularly notice that PGA greatly benefits from lens distortion estimation. This underlines our observation that the latter is essential for highly accurate segmentation.

Table 3: Pixelwise classification scores for quadrilateral masks estimated using PGA and the proposed approach. Bold face denotes the best performing method.

(a) Monocrystalline			
Metric	PGA		Proposed (quadrilateral)
	distorted	undistorted	
Precision	97.94 %	98.48 %	99.42 %
Recall	97.93 %	98.51 %	96.58 %
F_1 score	97.94 %	98.49 %	97.98 %
Accuracy	98.32 %	98.82 %	98.45 %
(b) Polycrystalline			
Metric	PGA		Proposed (quadrilateral)
	distorted	undistorted	
Precision	97.45 %	98.37 %	99.40 %
Recall	97.94 %	99.35 %	99.53 %
F_1 score	97.70 %	98.86 %	99.47 %
Accuracy	97.27 %	98.68 %	99.38 %
(c) Overall			
Metric	PGA		Proposed (quadrilateral)
	distorted	undistorted	
Precision	97.69 %	98.42 %	99.41 %
Recall	97.94 %	98.94 %	98.12 %
F_1 score	97.81 %	98.68 %	98.76 %
Accuracy	97.87 %	98.76 %	98.84 %

Pixelwise Classification Pixelwise scores for the simplified masks of both methods are given in Table 3. For monocrystalline PV modules, PGA generally achieves higher scores. However, highest scores are achieved only for images for which the lens distortion has been removed. The proposed method fails to segment a row of cells in a solar module resulting in a lower recall. However, for polycrystalline PV modules, the proposed method consistently outperforms PGA. In the overall score, the proposed method also outperforms the

Table 4: Pixelwise classification scores for exact masks estimated using the proposed approach

Metric	Monocrystalline	Polycrystalline	Overall
Precision	97.67 %	97.53 %	97.59 %
Recall	95.83 %	98.94 %	97.50 %
F_1 score	96.74 %	98.23 %	97.54 %
Accuracy	97.68 %	98.00 %	97.81 %

best-case evaluation for PGA on undistorted images. However, PGA has highest recall, which is due to the lower number of parameters of PGA.

Weighted Jaccard Index The Jaccard scores summarized as boxplots in Fig. 10 support the pixelwise classification scores, showing that the proposed method is more accurate than PGA. The latter, however, is slightly more robust. For complete modules, the considerable spread of PGA is partially attributed to one major outlier. Overall, the proposed segmentation pipeline is highly accurate. Particularly once a cell is detected, the cell outline is accurately and robustly segmented.

4.3.2 Segmentation Performance with Exact Cell Masks

To allow an exact comparison of the segmentation results to the ground truth, we inverse-warp the estimated solar cell masks back to the original image space by using the determined perspective projection and lens distortion parameters. This way, the estimated solar module masks will as exactly as possible overlay the hand-labeled ground truth masks.

Pixelwise Classification Table 4 summarizes the pixelwise classification scores for the exact masks estimated using the proposed method. The method is more robust on polycrystalline PV modules than on monocrystalline modules. However, for both module types, the method achieves a very high overall accuracy beyond 97 % for all metrics. Investigation of failure cases for monocrystalline modules reveals difficulties on cells where large gaps coincide with cell cracks and ragged edges.

Weighted Jaccard Index Jaccard scores for exact masks are given in Fig. 11. The scores confirm the results of the pixelwise metrics. Notably, the interquartile range (IQR) of individual cells has a very small spread, which indicates a highly consistent segmentation. The IQR of whole modules is slightly larger. This is, however, not surprising since the boxplots summarize the joint segmentation scores across multiple modules.

4.4 Qualitative Results

Figure 12 shows the qualitative results of the segmentation pipeline on four test images. The two results in the left column are computed on monocrystalline modules, the two results in the right column on polycrystalline modules. The estimated solar module curve grids are highly accurate. Even in presence of complex texture intrinsic to the material, the accuracy of the predicted solar module curve grid is not affected.

4.5 Runtime Evaluation

Figure 13 breaks down the average time taken by the individual steps of the segmentation pipeline. Figure 14 summarizes the contribution of individual pipeline steps to the overall processing time for all 44 images. The timings were obtained on a consumer system with an Intel i7-3770K CPU clocked at 3.50 GHz and 32 GB of RAM. The first three stages of the segmentation pipeline are implemented in C++ whereas the last stage (except for moving least squares image deformation) is implemented in Python.

For this benchmark, EL images were processed sequentially running only on the CPU. Note, however, that the implementation was not optimized in terms of the runtime and only parts of the pipeline utilize all available CPU cores. To this end, additional speedup can be achieved by running parts of the pipeline in parallel or even on a GPU.

On average, it takes 1 min and 6 s to segment all solar cells in a high resolution EL image (*cf.*, Fig. 14). Preprocessing is computationally most expensive, curve and cell extraction are on average cheapest. The standard deviation of the model estimation step is highest (see Fig. 13), which is mostly due to dependency upon the total number of ridge edges and the number of resulting curves combined with the probabilistic nature of LO-RANSAC.

Interestingly, processing EL images of monocrystalline solar modules takes slightly longer on average than processing polycrystalline solar modules. This is due to large gaps between ridges caused by cut-off edges that produce many disconnected curve segments which must be merged first. Conversely, curve segments in polycrystalline solar modules are closer, which makes it more likely that several curve segments are combined early on.

4.6 Limitations

Mounts that hold PV modules may cause spurious ridge edges. Early stages of the segmentation focus on ridges

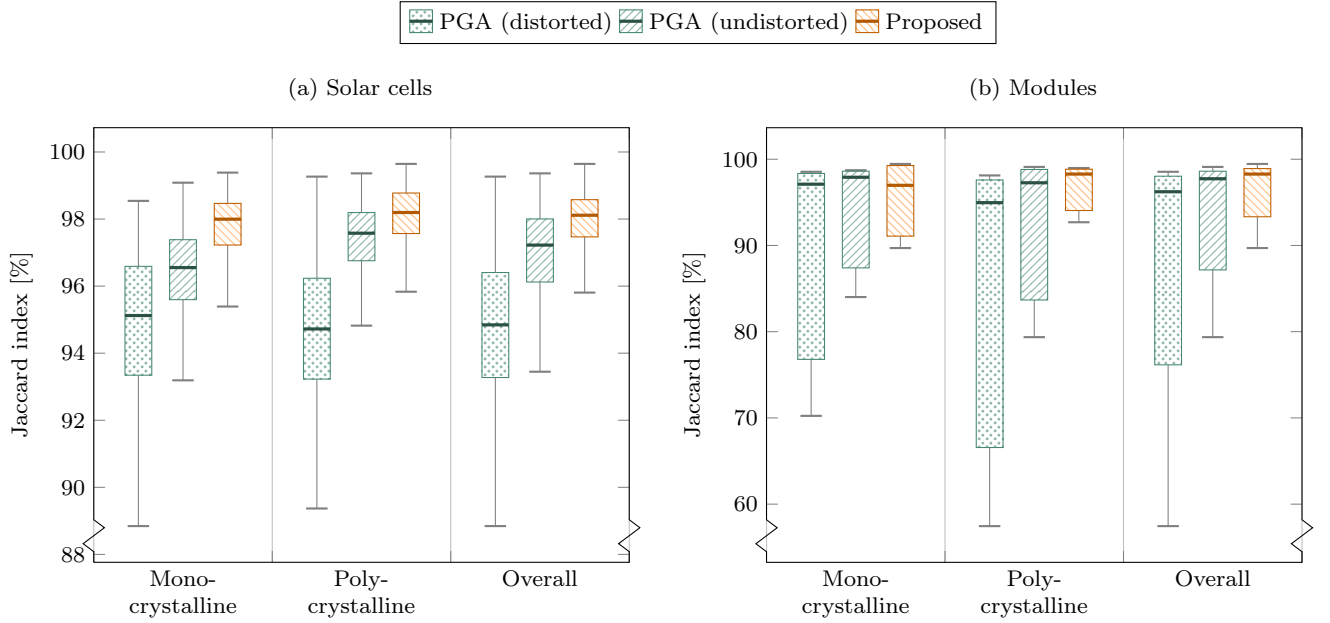


Figure 10: Boxplots of Jaccard scores for the three evaluated modalities. The Jaccard scores are computed against hand-labeled ground truth masks. In (a), the scores are computed for the individual solar cells. In (b), the scores are evaluated against the whole solar modules. The two left-most groups in each figure correspond to boxplots with respect to different solar wafers. Whereas the right-most group summarizes the performance of both solar wafer types combined.

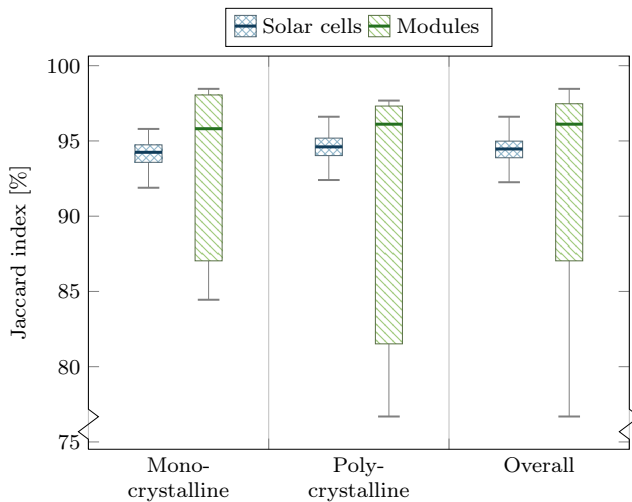


Figure 11: Boxplots of Jaccard scores for the proposed approach

without analyzing the whole image content, which may occasionally lead to spurious edges and eventually to an incorrect segmentation. Therefore, automatic image cropping prior to PV module segmentation could help reduce segmentation failures due to visible mounts.

While the algorithm is able to process disconnected (dark) cells, rows or columns with more than 50 % of

disconnected cells pose a difficulty in correctly detecting the grid due to insufficient edge information. However, we observed that also human experts have problems to determine the contours under such circumstances.

We also observed that smooth edges can result in segmentation failures. This is because the stickiness of smooth edges is weak and may completely fade away after non-maximum suppression. This problem is also related to situations where the inter-cell borders are exceptionally wide. In such cases, it is necessary to adjust the parameters of the ridgeness filter and the proximity of the tensor voting.

5 Conclusions

In this work, we presented a fully automatic segmentation method for precise extraction of solar cells from high resolution EL images. The proposed segmentation is robust to underexposure, and works robustly in presence of severe defects on solar cells. This can be attributed to the proposed preprocessing and the ridgeness filtering, coupled with tensor voting to robustly determine the inter-cell borders and busbars. The segmentation is highly accurate, which allows to use its output for further inspection tasks, such as automatic classification of defective solar cells and the prediction of power loss.

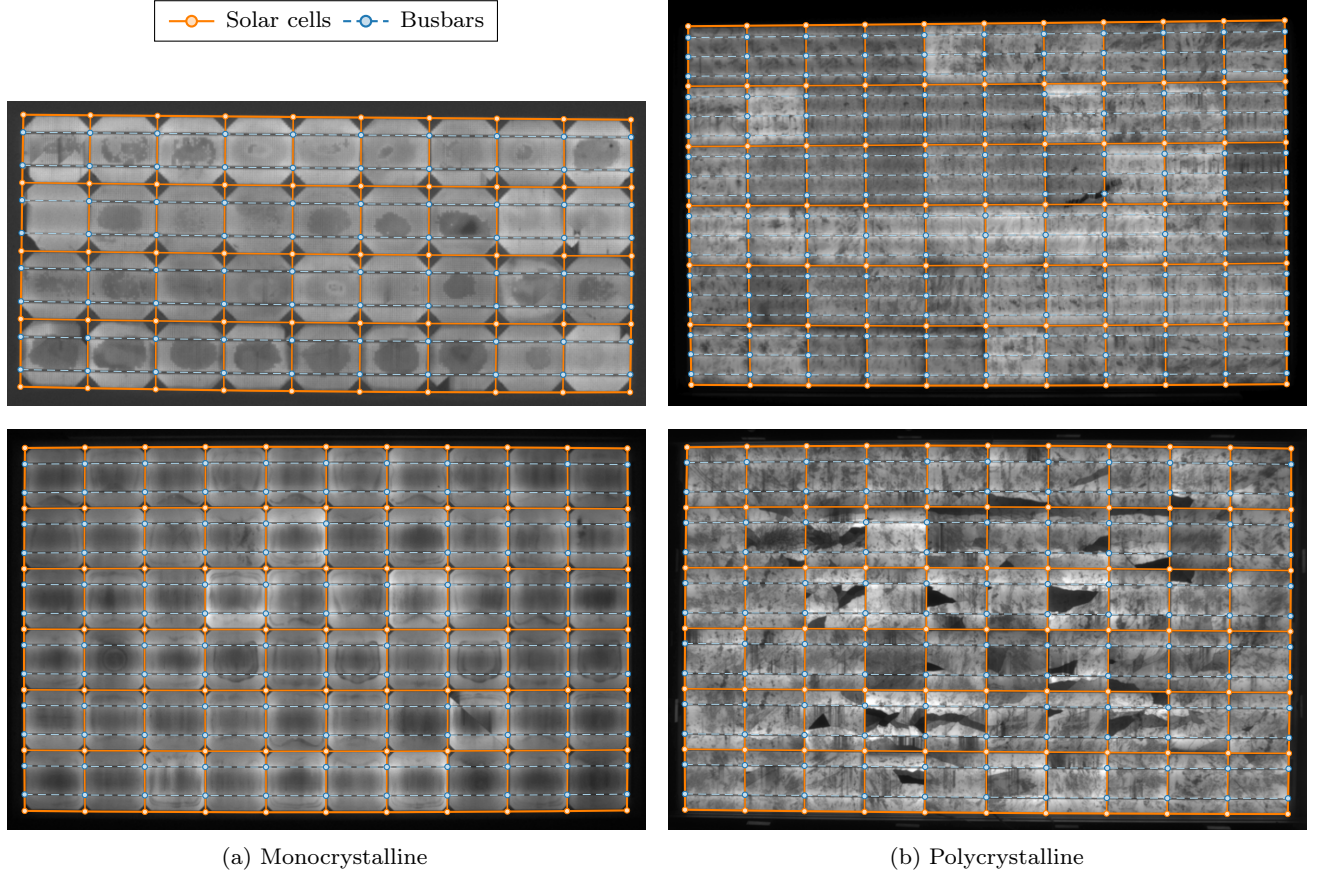


Figure 12: Qualitative segmentation results of four test images depicting the estimated curve grid superimposed over the contrast-normalized input EL image. For visualization purposes, the original EL images were cropped.

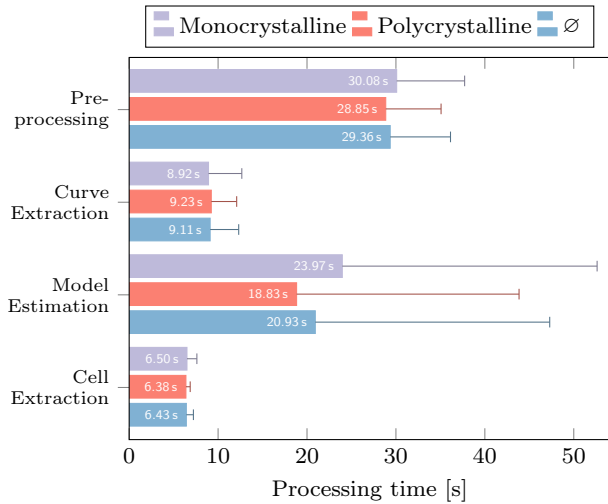


Figure 13: Average time taken by individual steps of the segmentation pipeline, in seconds. The error bars denote the upper range of the standard deviation.

We evaluated the segmentation in terms of the Jaccard index on eight different PV modules consisting of 408 hand-labeled solar cells. The proposed approach is

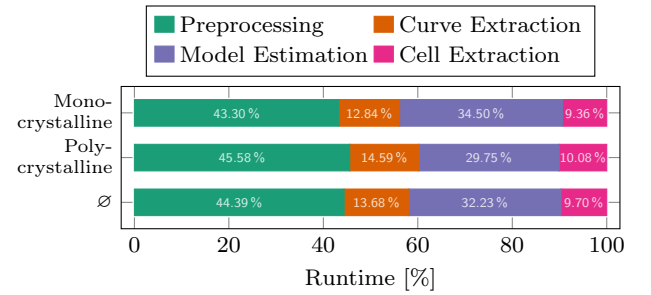


Figure 14: Relative contribution of the average processing time for individual pipeline steps to the overall runtime with respect to different solar module types and both types combined.

able to segment solar cells with an accuracy of 94.47%. In terms of classification performance, the segmentation pipeline reaches an F_1 score of 97.54%. Additionally, we compared the proposed method against the PV module detection approach by Sovetkin and Steland [69], which is slightly more robust but less accurate than our method.

Beyond the proposed applications, the method can serve as a starting point for bootstrapping deep learning architectures that could be trained end-to-end to directly segment the solar cells. Future work may include to investigate the required adaptations and geometric relaxations for using the method not only in manufacturing setting but also in the field.

Acknowledgements This work was funded by Energy Campus Nuremberg (EnCN) and partially supported by the Research Training Group 1773 “Heterogeneous Image Systems” funded by the German Research Foundation (DFG).

References

1. Aggarwal A, Chang JS, Yap CK (1985) Minimum area circumscribing polygons. *The Visual Computer* 1(2):112–117, DOI: [10.1007/BF01898354](#) 13, 15
2. Aloimonos J (1988) Shape from texture. *Biological Cybernetics* 58(5):345–360, DOI: [10.1007/BF00363944](#) 2
3. Anwar SA, Abdullah MZ (2014) Micro-crack detection of multicrystalline solar cells featuring an improved anisotropic diffusion filter and image segmentation technique. *EURASIP Journal on Image and Video Processing* 2014(1):15, DOI: [10.1186/1687-5281-2014-15](#) 1
4. Barber CB, Dobkin DP, Dobkin DP, Huhdanpaa H (1996) The quickhull algorithm for convex hulls. *ACM Transactions on Mathematical Software* 22(4):469–483, DOI: [10.1145/235815.235821](#) 12
5. Breitenstein O, Bauer J, Bothe K, Hinken D, Müller J, Kwapil W, Schubert MC, Warta W (2011) Can luminescence imaging replace lock-in thermography on solar cells? *IEEE Journal of Photovoltaics* 1(2):159–167, DOI: [10.1109/JPHOTOV.2011.2169394](#) 1
6. Brown DC (1971) Close-range camera calibration. *Photogrammetric Engineering & Remote Sensing* 37:855–866, DOI: [10.1.1.14.6358](#) 3, 7
7. Buerhop-Lutz C, Deitsch S, Maier A, Gallwitz F, Berger S, Doll B, Hauch J, Camus C, Brabec CJ (2018) A benchmark for visual identification of defective solar cells in electroluminescence imagery. In: 35th European PV Solar Energy Conference and Exhibition, pp 1287–1289, DOI: [10.4229/35thEUPVSEC20182018-5CV.3.15](#) 1
8. Chenni R, Makhoul M, Kerbach T, Bouzid A (2007) A detailed modeling method for photovoltaic cells. *Energy* 32(9):1724–1730, DOI: [10.1016/j.energy.2006.12.006](#) 1
9. Chierichetti F, Kumar R, Pandey S, Vassilvitskii S (2010) Finding the Jaccard median. In: *Symposium on Discrete Algorithms*, Austin, Texas, pp 293–311 14
10. Chum O, Matas J, Kittler J (2003) Locally optimized RANSAC. In: Michaelis B, Krell G (eds) *Pattern Recognition*, Springer, Berlin, Heidelberg, vol 2781, pp 236–243, DOI: [10.1007/978-3-540-45243-0_31](#) 11
11. Claus D, Fitzgibbon AW (2005) A plumblin constraint for the rational function lens distortion model. In: *British Machine Vision Conference (BMVC)*, pp 99–108, DOI: [10.5244/C.19.10](#) 3
12. Claus D, Fitzgibbon AW (2005) A rational function lens distortion model for general cameras. In: *Conference on Computer Vision and Pattern Recognition (CVPR)*, vol 1, pp 213–219, DOI: [10.1109/CVPR.2005.43](#) 3
13. Deitsch S, Christlein V, Berger S, Buerhop-Lutz C, Maier A, Gallwitz F, Riess C (2019) Automatic classification of defective photovoltaic module cells in electroluminescence images. *Solar Energy* 185:455–468, DOI: [10.1016/j.solener.2019.02.067](#), [1807.02894](#) 1
14. Devernay F, Faugeras O (2001) Straight lines have to be straight. *Machine Vision and Applications* 13(1):14–24, DOI: [10.1007/PL00013269](#) 3, 7, 10
15. Douglas DH, Peucker TK (1973) Algorithms for the reduction of the number of points required to represent a digitized line or its caricature. *Cartographica: The International Journal for Geographic Information and Geovisualization* 10(2):112–122, DOI: [10.3138/fm57-6770-u75u-7727](#) 6
16. Ester M, Kriegel HP, Sander J, Xu X, et al. (1996) A density-based algorithm for discovering clusters in large spatial databases with noise. In: *Proceedings of the Second International Conference on Knowledge Discovery and Data Mining*, AAAI Press, Portland, Oregon, vol 96, pp 226–231 11
17. Fabijańska A (2012) A survey of subpixel edge detection methods for images of heat-emitting metal specimens. *International Journal of Applied Mathematics and Computer Science* 22(3):695–710, DOI: [10.2478/v10006-012-0052-3](#) 6
18. Fischler MA, Bolles RC (1981) Random sample consensus: A paradigm for model fitting with applications to image analysis and automated cartography. *Communications of the ACM* 24(6):381–395, DOI: [10.1145/358669.358692](#) 7
19. Fitzgibbon A (2001) Simultaneous linear estimation of multiple view geometry and lens distortion. In: *IEEE Computer Society Conference on Computer Vision and Pattern Recognition*, IEEE, vol 1, pp 125–132, DOI: [10.1109/CVPR.2001.990465](#) 3

20. Flocke N (2015) Algorithm 954: An accurate and efficient cubic and quartic equation solver for physical applications. *ACM Transactions on Mathematical Software* 41(4):30:1–30:24, DOI: [10.1145/2699468.9](https://doi.org/10.1145/2699468.9)
21. Franken E, van Almsick M, Rongen P, Florack L, ter Haar Romeny B (2006) An efficient method for tensor voting using steerable filters. In: Leonardis A, Bischof H, Pinz A (eds) *European Conference on Computer Vision (ECCV)*, pp 228–240, DOI: [10.1007/11744085_18](https://doi.org/10.1007/11744085_18) 5
22. Franken E, Rongen P, van Almsick M, ter Haar Romeny B (2006) Detection of electrophysiology catheters in noisy fluoroscopy images. In: Larsen R, Nielsen M, Sporrang J (eds) *Medical Image Computing and Computer-Assisted Intervention – MICCAI 2006*, Springer, Berlin, Heidelberg, pp 25–32, DOI: [10.1007/11866763_4](https://doi.org/10.1007/11866763_4) 4, 5
23. Fürsattel P, Dotenco S, Placht S, Balda M, Maier A, Riess C (2016) OCPAD – occluded checkerboard pattern detector. In: *Winter Conference on Applications of Computer Vision (WACV)*, IEEE, DOI: [10.1109/WACV.2016.7477565](https://doi.org/10.1109/WACV.2016.7477565) 3
24. Girshick RB (2015) Fast R-CNN. In: *IEEE International Conference on Computer Vision*, pp 1440–1448, DOI: [10.1109/ICCV.2015.169](https://doi.org/10.1109/ICCV.2015.169) 3
25. Girshick RB, Donahue J, Darrell T, Malik J (2014) Rich feature hierarchies for accurate object detection and semantic segmentation. In: *IEEE Conference on Computer Vision and Pattern Recognition*, pp 580–587, DOI: [10.1109/CVPR.2014.81](https://doi.org/10.1109/CVPR.2014.81) 3
26. Golub GH, Van Loan CF (2013) *Matrix Computations*, 4th edn. Johns Hopkins Studies in the Mathematical Sciences, Johns Hopkins University Press 4, 7, 9
27. Gonzalez RC, Woods RE (2018) *Digital Image Processing*, 4th edn. Pearson, New York, NY, USA 4
28. Ha H, Perdoch M, Alismail H, Kweon IS, Sheikh Y (2017) Deltile grids for geometric camera calibration. In: *International Conference on Computer Vision (ICCV)*, pp 5354–5362, DOI: [10.1109/ICCV.2017.571](https://doi.org/10.1109/ICCV.2017.571) 3
29. Harker M, O’Leary P, Zsombor-Murray P (2008) Direct type-specific conic fitting and eigenvalue bias correction. *Image and Vision Computing* 26(3):372–381, DOI: [10.1016/j.imavis.2006.12.006](https://doi.org/10.1016/j.imavis.2006.12.006) 7
30. Hartley R, Zisserman A (2004) *Multiple View Geometry in Computer Vision*, 2nd edn. Cambridge University Press, New York, NY, USA 7, 12
31. He K, Gkioxari G, Dollár P, Girshick RB (2017) Mask R-CNN. In: *IEEE International Conference on Computer Vision*, pp 2980–2988, DOI: [10.1109/ICCV.2017.322](https://doi.org/10.1109/ICCV.2017.322) 3
32. He X, Zemel RS, Carreira-Perpinan MA (2004) Multiscale conditional random fields for image labeling. In: *Conference on Computer Vision and Pattern Recognition*, IEEE, vol 2, pp 695–702, DOI: [10.1109/CVPR.2004.1315232](https://doi.org/10.1109/CVPR.2004.1315232) 12
33. Hoffmann M, Ernst A, Bergen T, Hettkenkofer S, Garbas JU (2017) A robust chessboard detector for geometric camera calibration. In: *International Joint Conference on Computer Vision, Imaging and Computer Graphics Theory and Applications (VISIGRAPP)*, pp 34–43, DOI: [10.5220/0006104300340043](https://doi.org/10.5220/0006104300340043) 3
34. IEC TS 60904-13:2018 (2018) Photovoltaic devices – part 13: Electroluminescence of photovoltaic modules. Technical specification, International Electrotechnical Commission 1
35. Ioffe S (2010) Improved consistent sampling, weighted minhash and L^1 sketching. In: *International Conference on Data Mining*, pp 246–255, DOI: [10.1109/ICDM.2010.80](https://doi.org/10.1109/ICDM.2010.80) 14
36. Jaderberg M, Simonyan K, Zisserman A, Kavukcuoglu K (2015) Spatial transformer networks. In: Cortes C, Lawrence ND, Lee DD, Sugiyama M, Garnett R (eds) *Advances in Neural Information Processing Systems*, 28, Curran Associates, Inc., pp 2017–2025 1
37. Jenkins MA, Traub JF (1970) A three-stage algorithm for real polynomials using quadratic iteration. *Journal on Numerical Analysis* 7(4):545–566, DOI: [10.1137/0707045](https://doi.org/10.1137/0707045) 9
38. Karatepe E, Boztepe M, Çolak M (2007) Development of a suitable model for characterizing photovoltaic arrays with shaded solar cells. *Solar Energy* 81(8):977–992, DOI: [10.1016/j.solener.2006.12.001](https://doi.org/10.1016/j.solener.2006.12.001) 1
39. Kaushika ND, Gautam NK (2003) Energy yield simulations of interconnected solar PV arrays. *IEEE Transactions on Energy Conversion* 18(1):127–134, DOI: [10.1109/TEC.2002.805204](https://doi.org/10.1109/TEC.2002.805204) 1
40. Kovesi P (2017) MATLAB and octave functions for computer vision and image processing. URL <http://www.peterkovesi.com/matlabfns> 6
41. Levenberg K (1944) A method for the solution of certain non-linear problems in least squares. *Quarterly of Applied Mathematics* 2(2):164–168 10
42. Li Y, Qi H, Dai J, Ji X, Wei Y (2017) Fully convolutional instance-aware semantic segmentation. In: *IEEE Conference on Computer Vision and Pattern Recognition*, pp 4438–4446, DOI: [10.1109/CVPR.2017.472](https://doi.org/10.1109/CVPR.2017.472) 3
43. Lin CH, Lucey S (2017) Inverse compositional spatial transformer networks. In: *IEEE Conference on Computer Vision and Pattern Recognition*

- (CVPR), IEEE, pp 2252–2260, DOI: [10.1109/CVPR.2017.242](#) 1
44. Lindeberg T (1994) Scale-space theory: A basic tool for analyzing structures at different scales. *Journal of Applied Statistics* 21(1-2):225–270, DOI: [10.1080/757582976](#) 4
 45. Lindeberg T (1996) Edge detection and ridge detection with automatic scale selection. In: *Proceedings of the Conference on Computer Vision and Pattern Recognition*, pp 465–470, DOI: [10.1109/CVPR.1996.517113](#) 4
 46. Lindeberg T (1998) Edge detection and ridge detection with automatic scale selection. *International Journal of Computer Vision* 30(2):117–156, DOI: [10.1023/A:1008097225773](#) 4
 47. Long J, Shelhamer E, Darrell T (2015) Fully convolutional networks for semantic segmentation. In: *Conference on Computer Vision and Pattern Recognition (CVPR)*, pp 3431–3440, DOI: [10.1109/CVPR.2015.7298965](#) 3
 48. Marquardt DW (1963) An algorithm for least-squares estimation of nonlinear parameters. *Journal of the Society for Industrial and Applied Mathematics* 11(2):431–441, DOI: [10.1137/0111030](#) 10
 49. Mauk MG (2013) Image processing for solar cell analysis, diagnostics and quality assurance inspection. In: *Image Processing: Concepts, Methodologies, Tools, and Applications*, IGI Global, chap 71, pp 1426–1462 1
 50. Medioni G, Tang CK, Lee MS (2000) Tensor voting: Theory and applications. In: *Proceedings of RFIA* 5
 51. Mehta S, Azad AP, Chemmengath SA, Raykar V, Kalyanaraman S (2018) DeepSolarEye: Power loss prediction and weakly supervised soiling localization via fully convolutional networks for solar panels. In: *Winter Conference on Applications of Computer Vision (WACV)*, pp 333–342, DOI: [10.1109/WACV.2018.00043](#) 3
 52. Myronenko A, Song X (2010) Point set registration: Coherent point drift. *IEEE Transactions on Pattern Analysis and Machine Intelligence* 32(12):2262–2275, DOI: [10.1109/TPAMI.2010.46](#) 11
 53. Nian B, Fu Z, Wang L, Cao X (2010) Automatic detection of defects in solar modules: Image processing in detecting. In: *2010 International Conference on Computational Intelligence and Software Engineering*, IEEE, pp 1–4, DOI: [10.1109/WICOM.2010.5600703](#) 1
 54. Nocedal J, Wright SJ (2006) *Numerical Optimization*, Operations Research and Financial Engineering, vol 43, 2nd edn. Springer, New York, USA, DOI: [10.1007/978-0-387-40065-5](#) 6
 55. Otsu N (1979) A threshold selection method from gray-level histograms. *IEEE Transactions on Systems, Man, and Cybernetics* 9(1):62–66, DOI: [10.1109/TSMC.1979.4310076](#) 6, 11
 56. Pitas I (1993) *Digital Image Processing Algorithms*. Prentice-Hall, Inc., Upper Saddle River, NJ, USA 12
 57. Placht S, Fürsattel P, Mengue EA, Hofmann H, Schaller C, Balda M, Angelopoulou E (2014) ROCHADE: Robust checkerboard advanced detection for camera calibration. In: *Fleet D, Pajdla T, Schiele B, Tuytelaars T (eds) European Conference on Computer Vision (ECCV), Lecture Notes in Computer Science*, vol 8692, pp 766–779, DOI: [10.1007/978-3-319-10593-2_50](#) 3
 58. Potthoff T, Bothe K, Eitner U, Hinken D, Köntges M (2010) Detection of the voltage distribution in photovoltaic modules by electroluminescence imaging. *Progress in Photovoltaics: Research and Applications* 18(2):100–106, DOI: [10.1002/pip.941](#) 1
 59. Prasad DK, Leung MKH, Quek C, Cho SY (2012) A novel framework for making dominant point detection methods non-parametric. *Image and Vision Computing* 30(11):843–859, DOI: [10.1016/j.imavis.2012.06.010](#) 6
 60. Quaschnig V, Hanitsch R (1996) Numerical simulation of current-voltage characteristics of photovoltaic systems with shaded solar cells. *Solar Energy* 56(6):513–520, DOI: [10.1016/0038-092X\(96\)00006-0](#) 1
 61. Ramer U (1972) An iterative procedure for the polygonal approximation of plane curves. *Computer Graphics and Image Processing* 1(3):244–256, DOI: [10.1016/S0146-664X\(72\)80017-0](#) 6
 62. Ren S, He K, Girshick R, Sun J (2017) Faster R-CNN: Towards real-time object detection with region proposal networks. *IEEE Transactions on Pattern Analysis and Machine Intelligence* 39(6):1137–1149, DOI: [10.1109/TPAMI.2016.2577031](#) 3
 63. van Rijsbergen CJ (1979) *Information Retrieval*, 2nd edn. Butterworth-Heinemann 14
 64. Ronneberger O, Fischer P, Brox T (2015) U-Net: Convolutional networks for biomedical image segmentation. In: *Navab N, Hornegger J, Wells WM, Frangi AF (eds) Medical Image Computing and Computer-Assisted Intervention – MICCAI 2015*, Springer, Cham, pp 234–241, DOI: [10.1007/978-3-319-24574-4_28](#) 3
 65. Rosten E, Loveland R (2011) Camera distortion self-calibration using the plumb-line constraint and minimal Hough entropy. *Machine Vision and Applications* 22(1):77–85, DOI: [10.1007/s00138-009-0196-9](#), [0810.4426](#) 3

66. Ruffi M, Scaramuzza D, Siegwart R (2008) Automatic detection of checkerboards on blurred and distorted images. In: International Conference on Intelligent Robots and Systems, pp 3121–3126, DOI: [10.1109/IROS.2008.4650703](https://doi.org/10.1109/IROS.2008.4650703) 3
67. Saeed K, Tabędzki M, Rybnik M, Adamski M (2010) K3M: A universal algorithm for image skeletonization and a review of thinning techniques. International Journal of Applied Mathematics and Computer Science 20(2):317–335, DOI: [10.2478/v10006-010-0024-4](https://doi.org/10.2478/v10006-010-0024-4) 6
68. Schaefer S, McPhail T, Warren J (2006) Image deformation using moving least squares. ACM Transactions on Graphics 25(3):533, DOI: [10.1145/1141911.1141920](https://doi.org/10.1145/1141911.1141920) 12
69. Sovetkin E, Steland A (2019) Automatic processing and solar cell detection in photovoltaic electroluminescence images. Integrated Computer-Aided Engineering 26(2):123–137, DOI: [10.3233/ICA-180588](https://doi.org/10.3233/ICA-180588) 3, 13, 14, 15, 18
70. Spataru S, Hacke P, Sera D (2016) Automatic detection and evaluation of solar cell micro-cracks in electroluminescence images using matched filters. In: 2016 IEEE 43rd Photovoltaic Specialists Conference (PVSC), pp 1602–1607, DOI: [10.1109/PVSC.2016.7749891](https://doi.org/10.1109/PVSC.2016.7749891) 12
71. Spertino F, Ciocia A, Leo PD, Tommasini R, Berardone I, Corrado M, Infuso A, Paggi M (2015) A power and energy procedure in operating photovoltaic systems to quantify the losses according to the causes. Solar Energy 118:313–326, DOI: [10.1016/j.solener.2015.05.033](https://doi.org/10.1016/j.solener.2015.05.033) 13
72. Stromer D, Vetter A, Oezkan HC, Probst C, Maier A (2019) Enhanced crack segmentation (eCS): A reference algorithm for segmenting cracks in multicrystalline silicon solar cells. IEEE Journal of Photovoltaics 9(3):752–758, DOI: [10.1109/JPHOTOV.2019.2895808](https://doi.org/10.1109/JPHOTOV.2019.2895808) 12
73. Tsai DM, Wu SC, Li WC (2012) Defect detection of solar cells in electroluminescence images using Fourier image reconstruction. Solar Energy Materials and Solar Cells 99:250–262, DOI: [10.1016/j.solmat.2011.12.007](https://doi.org/10.1016/j.solmat.2011.12.007) 1
74. Tsai DM, Wu SC, Chiu WY (2013) Defect detection in solar modules using ICA basis images. IEEE Transactions on Industrial Informatics 9(1):122–131, DOI: [10.1109/TII.2012.2209663](https://doi.org/10.1109/TII.2012.2209663) 1
75. Tsai RY (1987) A versatile camera calibration technique for high-accuracy 3D machine vision metrology using off-the-shelf TV cameras and lenses. IEEE Journal on Robotics and Automation 3(4):323–344, DOI: [10.1109/JRA.1987.1087109](https://doi.org/10.1109/JRA.1987.1087109) 7
76. Tseng DC, Liu YS, Chou CM (2015) Automatic finger interruption detection in electroluminescence images of multicrystalline solar cells. Mathematical Problems in Engineering 2015:1–12, DOI: [10.1155/2015/879675](https://doi.org/10.1155/2015/879675) 1